Applied Energy 380 (2025) 125042

Contents lists available at ScienceDirect

Applied Energy

journal homepage: www.elsevier.com/locate/apenergy

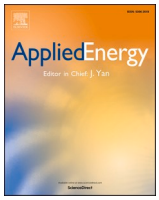

# Experimental demonstration and validation of tubular solar cavity receivers for simultaneous generation of superheated steam and hot air

Yasuki Kadohiro [a,*], Timo Roeder [a,b], Kai Risthaus [a], Dmitrij Laaber [a], Nathalie Monnerie [a], Christian Sattler [a,b]

[a] Deutsches Zentrum für Luft- und Raumfahrt, Institute of Future Fuels, Linder Höhe, 51147, Cologne, Germany
[b] RWTH Aachen University, Chair for Solar Fuel Production, Aachen, Germany

## HIGHLIGHTS

- Solar receiver concept for simultaneous generation of high-temperature air and steam.
- Experimental demonstration of solar cavity receiver with 70 $kW_{th}$ nominal power.
- Proposed receiver could continuously produce hot steam (811 °C) and hot air (863 °C).
- Numerical model developed was validated with a relative error of less than 10 %.
- Great coupling potential for solar receivers and high-temperature electrolysis.

## ARTICLE INFO

*Keywords::*
Solar cavity receiver
Helical absorber tubes
Superheated steam
Hot air
Experimental demonstration
Green hydrogen

## ABSTRACT

Cavity receivers with absorber tubes inside the solar tower systems are the most studied and suitable concept for supplying such hot steam and air due to its design flexibility and efficiency. However, a receiver concept of simultaneously generating high-temperature steam and air has not been experimentally studied on scales beyond laboratory scale. Therefore, our study focused on the experimental demonstration for such receiver concept and the validation of the developed numerical model. Experimental results demonstrated that the proposed receiver concept (i.e. a cavity receiver with cylindrical and conical helical tubes) with 70 $kW_{th}$ nominal power can simultaneously produce high-temperature steam (811 °C) and air (863 °C) with standard deviations of less than 3 °C (outlet temperature), 3 kPa (outlet pressure), and 0.2 kg/h (mass flow rate). Comparison of experiments and simulations proved to be in very good agreement, with errors of less than 10 %. The results presented here provide a basis for future scale-up and demonstrate the high potential of combining concentrating solar thermal technology with high-temperature electrolysis for the mass production of green hydrogen.

## 1. Introduction

Concentrated solar thermal (CST) technology can provide high-temperature heat that can be used for a variety of applications, such as industrial process heat, power generation, and fuel production (e.g., hydrogen, methanol, and diesel). Among these applications, heat used for fuel production requires a temperature above 600 °C, which can be generated by point-focussing solar concentrators, especially solar tower systems in large-scale plant operations [1].

Examples of fuel production (focusing on hydrogen) in solar tower systems include: (1) hybrid sulfur cycles [2,3], (2) high-temperature electrolysis (HTE) [4,5], and (3) redox-pair oxide systems [6,7]. Among these approaches, the solar hydrogen production via HTE is attractive since it does not use highly toxic chemicals (only steam and air), can operate at relatively low temperatures compared to the other options cited, and is relatively energy efficient for hydrogen production compared to the other approaches [8]. Furthermore, HTE can reduce electricity consumption in comparison with other electrolysis processes

*Abbreviation:* AT, absorber tube; CSP, concentrated solar power; CST, concentrated solar thermal; EW, evaporating water; FEMRAY, finite element mesh ray tracing; FMAS, flux mapping acquisition system; HA, heating air; HTE, high-temperature electrolysis; SS, superheating steam; TES, thermal energy storage.

* Corresponding author.
*E-mail address:* Yasuki.Kadohiro@dlr.de (Y. Kadohiro).

https://doi.org/10.1016/j.apenergy.2024.125042
Received 29 August 2024; Received in revised form 28 October 2024; Accepted 27 November 2024
Available online 2 December 2024

by supplying heat at high temperatures (700–1000 °C), and can achieve much higher electrical efficiency than alkaline electrolysis at low temperatures (below 100 °C) [9]. However, the scale-up of equipment remains an important research issue, as there are several difficulties in achieving multi-MW scale HTE, including very few experimental data at higher kW levels and few operating strategies for multi-MW scale HTE plants [10,11].

Solar tower systems consist primarily of a large number of heliostats (i.e., mirrors that track the sun), a receiver that converts the light collected from the heliostats into thermal energy, a tower that is necessary to place the receivers at the proper height, and optionally a thermal energy storage (TES) that is necessary to store excess heat and enable the nighttime as well as continuous operation during cloud shading periods [12,13]. The receiver is one of the key components of the system and can be classified into two types: (1) cavity type and (2) external type. The cavity type mounts the absorber inside a cavity with an opening, while the external type mounts the absorber outside [14]. Although the cavity type is implemented less frequently (around 30 %), it is gaining more attention than the external type because of its significantly lower radiation loss [15,16] and a higher annual optical efficiency of 10 % or more compared to external receivers [17]. Furthermore, cavity receivers can also reduce convective losses in contrast to external types, especially in the presence of strong winds (forced convection) [16].

Detailed studies of such cavity receivers are ongoing, and various designs are being investigated for optimization [18,19] and different purposes [20]. For the high-temperature steam and air generations, cavity receivers with absorber tubes (ATs) are the most studied designs since they offer greater design flexibility and are more efficient than other designs [14]. Such tubular cavity receivers are mainly applied to concentrating solar power (CSP) plants for power generation [13,21], and more recently to solar tower systems combined with HTE [9,22].

Quero et al. [23] have experimentally demonstrated the tubular cavity receiver concept for high-temperature air production. They deployed 170 fine nickel-based alloy straight tubes inside the cavity and showed that the designed receiver concept can produce pressurized air (1 MPa, absolute) at 800 °C with Abengoa's solar tower systems. Qiu et al. [24] also experimentally studied the cavity receiver employing a 15-turn helical coil tube (with cylindrical shape) for high-temperature air production. Their study demonstrated the concept of supplying heated air up to 662 °C with five 7 $kW_e$ Xe-arc lamps. Chu et al. [25] experimentally demonstrated the tubular receiver concept deploying double helical tubes (with conical shape) for heated air generation. A solar furnace system was used as the light source, proving that the proposed concept can obtain high-temperature pressurized (0.6 MPa, absolute) air at 900 °C.

Houaijia et al. [22] have experimentally studied the cavity receiver consisting of multiple straight ATs for superheating steam. Their study proved that the constructed receiver can produce superheated steam at 700 °C with a solar simulator input of about 4 $kW_{rad}$. Schiller et al. [9] experimentally demonstrated the concept coupling solar steam generator with the HTE. They designed the cavity receiver with a helical AT (with conical shape) to evaporate water and superheat steam at once. Their study has shown that the designed tubular cavity receiver can produce high-temperature steam up to 700 °C with two 7 $kW_e$ Xe-arc lamps. Lin et al. [26] also experimentally investigated the cavity receiver concept employing a helical AT (with cylindrical shape). The cutting edge of their receiver design was the incorporation of HTE into the cavity. Their experimental study used up to six 2.5 $kW_e$ Xe-arc lamps to demonstrate the generation of hot air (sweep gas) and steam at 800 °C.

Various tubular cavity receiver designs for high-temperature steam and air production have been experimentally studied to validate the numerical model developed and to provide a practical proof of concept. However, research on the concept of tubular cavity receivers capable of simultaneously generating high-temperature steam and air is scarce as shown above and there are currently no experimental studies on this concept on scales beyond a few kW.

Our study focuses on the experimental demonstration of an upscaled tubular solar cavity receiver for simultaneous generation of superheated steam and hot air. The receiver concept with 70 $kW_{th}$ nominal power has been developed and tested for several days in quasi-steady state conditions using a solar simulator. Furthermore, this study focuses on the validation of the coupled 1D—3D numerical models developed in our previous studies [27,28]. The simulation results were compared with the obtained experimental data and relative errors were calculated. A parameter study was also conducted by varying several boundary conditions to investigate their impact on the receiver's performance. Furthermore, the receiver efficiency was compared with existing literature to demonstrate the effectiveness of the proposed solar cavity receiver concept.

## 2. Experimental setup

### 2.1. Process flow diagram

Fig. 1 shows the process flow diagram of the experiment. Note that the pressure shown in the figure is absolute pressure (a).

It can be seen from the figure that there are mainly three components: (1) solar cavity receiver, (2) packed bed TES, and (3) steam accumulator. Since the paper focuses on the solar cavity receiver, the details of TES, including the processes involved in it, are not presented. However, those details can be seen from the work done by Roeder et al. [29] and their future work on the experimental and numerical evaluations of the packed bed TES. The solar cavity receiver was used to produce three different fluids: (i) middle temperature steam (< 400 °C, Evaporating water (EW) section), (ii) high-temperature steam (< 820 °C, Superheating steam (SS) section), and (iii) high-temperature air (< 850 °C, Heating air (HA) section). Therefore, three different helical ATs are incorporated inside the receiver. The detailed structure is explained in Section 2.3. The heat flux was supplied by the solar simulator "Synlight" to heat the fluid in the receiver. The solar simulator consists of 148 Xenon short-arc lamps and can provide maximum 300–400 kW thermal load [30]. The detailed thermal load and heat flux distribution provided from the solar simulator are shown in Section 3. The TES was used to store the heat provided from the solar cavity receiver. The steam accumulator was used for temporary storage of saturated steam. Separating the water evaporation process from the steam superheating process allows for safer, more economical, and easier system operation [31].

Temperature sensors (TR) using type N thermocouples and gauge pressure sensors (PR) were installed at the inlet and outlet of the receiver and TES, in order to measure fluid temperature and pressure. Two mass flow controllers (FRC) were placed at the inlet of the water evaporation section and the heating air section to measure and adjust the mass flow rate of water and air. One mass flow meter was installed at the inlet of the superheating steam section to measure the mass flow rate of middle temperature steam. Check valves (CV) were incorporated into the process to avoid the fluid backflow. A back pressure regulator (BPR) was installed after the water mass flow controller to avoid fluctuations in water mass flow rate and pressure. A solenoid valve (SV), a ball valve with actuator (BVA), and needle valves with actuators (NVA) were incorporated to remotely control the fluid flow in the process. During the startup phase, the solenoid valve (SV) was opened and the ball valve with actuator (BVA) was closed to allow air flow into the SS section because to avoid overheating as there was no steam stored in the steam accumulator, yet. When there was sufficient steam in the steam accumulator, the solenoid valve (SV) and ball valve with actuator (BVA) were switched. The first and second needle valves with actuator (NVA-1 and NVA-2) were turned on when only the solar cavity receiver was tested, while the first and third needle valves with actuator (NVA-1 and NVA-3) were turned on when the charging of TES was tested. A needle

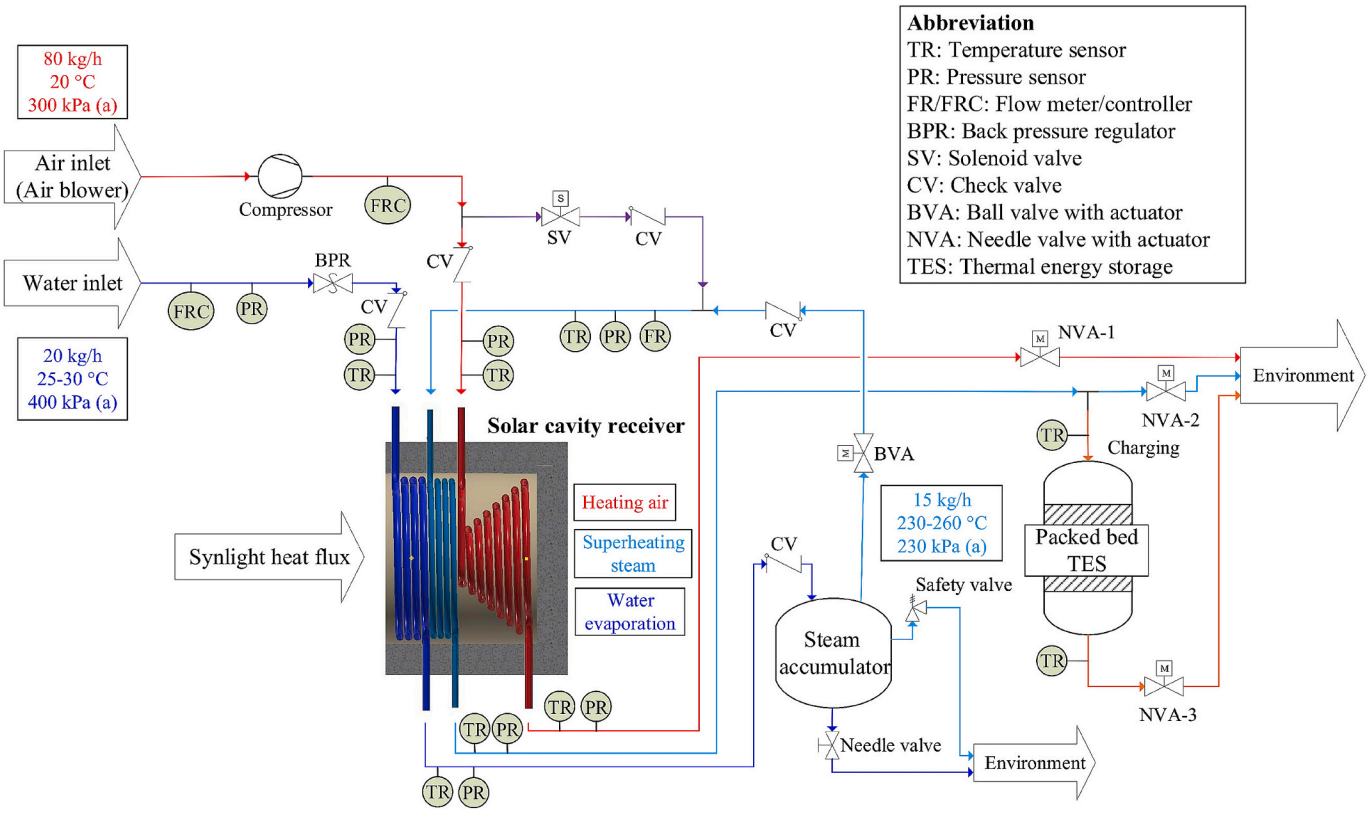


**Fig. 1.** Process flow diagram of the experiment.

valve and a safety valve were installed near the steam accumulator to discharge the water remaining in the vessel after the experiment and to discharge the steam if the internal pressure becomes higher than 300 kPa (a), respectively. A compressor was used for the air flow to pressurized the air up to 300 kPa (a).

The main objective of the experiment shown in Fig. 1 was to generate high-temperature air and steam (> 800 °C) from the solar cavity receiver continuously in a steady-state condition. The produced high-temperature fluids were cooled down and then sent to the environment. However, in a practical case, it is assumed that those high-temperature fluids are used directly on both the anode and cathode sides of HTE to produce green hydrogen and sweep the gas, respectively. The role of the TES in this case is to allow continuous operation or hot standby of the HTE during the hours when the sun is not shining or blocked by clouds. The inlet conditions of water and air flow shown in Fig. 1 were decided based on our numerical studies [28] and practical considerations.

Fig. 2 shows a photograph of the actual experimental setup. The three main components, (1) solar cavity receiver, (2) TES, (3) steam accumulator, and the solar simulator "Synlight" are shown. In addition, a radiation shield was added to cover the entire setup except for the cavity receiver's aperture to avoid damage from the concentrated irradiation of the lamps. The measurement and control equipments (e.g., mass flow meter, mass flow controller) were covered with aluminum foil

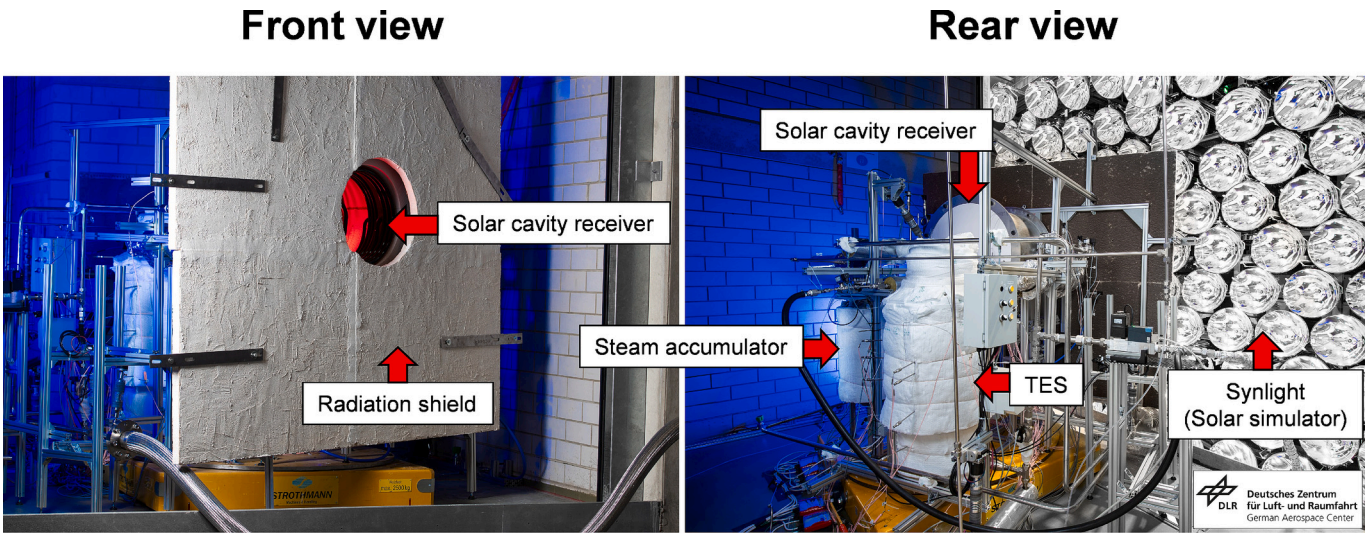


**Fig. 2.** Photograph of the actual experimental setup.

to reflect scattered light and avoid any impact (such as changes in measurement values) on the devices.

### 2.2. "Synlight" lamps and receiver position

Fig. 3 shows the actual lamps' location and receiver position used in the experiment. The diagram on the left shows the 148 xenon short-arc lamps in the Synlight facility, while the diagram on the right shows the position of the receiver in the facility.

As shown in the figure, 29 lamps were used in the experiment to provide enough power to the cavity receiver. The right side lamps (lamp numbers 7 through 12) were primarily used since the receiver was located in the right side of "Synlight" solar simulator. The distance between the solar simulator and receiver's aperture center, the vertical distance between the center line of solar simulator and receiver's aperture center, and the horizontal distance between the center line of solar simulator and receiver's aperture center were 6.13 m, 0.55 m, and 4.62 m, respectively. The cavity receiver was tilted horizontally at 25° to capture the light efficiently.

The focal points of all 29 lamps were within the range of the receiver's aperture, but they were not at the same point. A muilt-point aiming strategy was adopted in the experiment to make the heat flux distribution in the cavity more uniform and avoid overheating the materials. This approach has recently attracted attention in solar tower systems since it can avoid the extremely high solar heat flux from heliostat fields [32].

### 2.3. Experimental design of solar cavity receiver

Fig. 4 shows the photograph of a solar cavity receiver built and tested.

The solar cavity receiver consists of five components: (i) Stainless steel housing, (ii) insulation, (iii) AT for EW section, (iv) AT for SS section, and (v) AT for HA section. The stainless steel housing is made of stainless steel 1.4301, and it is used to cover and fix the insulation materials. Moreover, it is used to prevent the insulation material's abrasion. The insulation is made of polycrystalline high-alumina wool, and it is used to cover three ATs and suppress heat losses from the cavity inner side. The stainless steel housing is divided into four parts and the insulation into five parts to facilitate installation. The details are described in Appendix A. Three helical ATs are incorporated inside the cavity receiver to allow three different processes as described in Section 2.1. The helical shape was adopted since it can highly resist against the thermal expansion [33] and transfer the heat effectively [34]. As shown in Fig. 4, the AT for HA section is placed in the back side of the cavity. This AT has a conical shape to absorb light more efficiently [35] and transfer the excess energy to the other ATs through the re-radiation phenomenon. The conical helical AT receives the most energy, and the HA section was assigned here because the mass flow rate of air is four times that of water and requires more energy. The other two ATs have a cylindrical shape, used primarily in many studies [18], and the AT for EW section is installed near the receiver aperture since it has the lowest operating temperature. The exact arrangement of each AT and the inlet conditions for each section can also be seen in Fig. 1. All ATs are made of high-temperature stainless steel 1.4841 and covered with black paint to

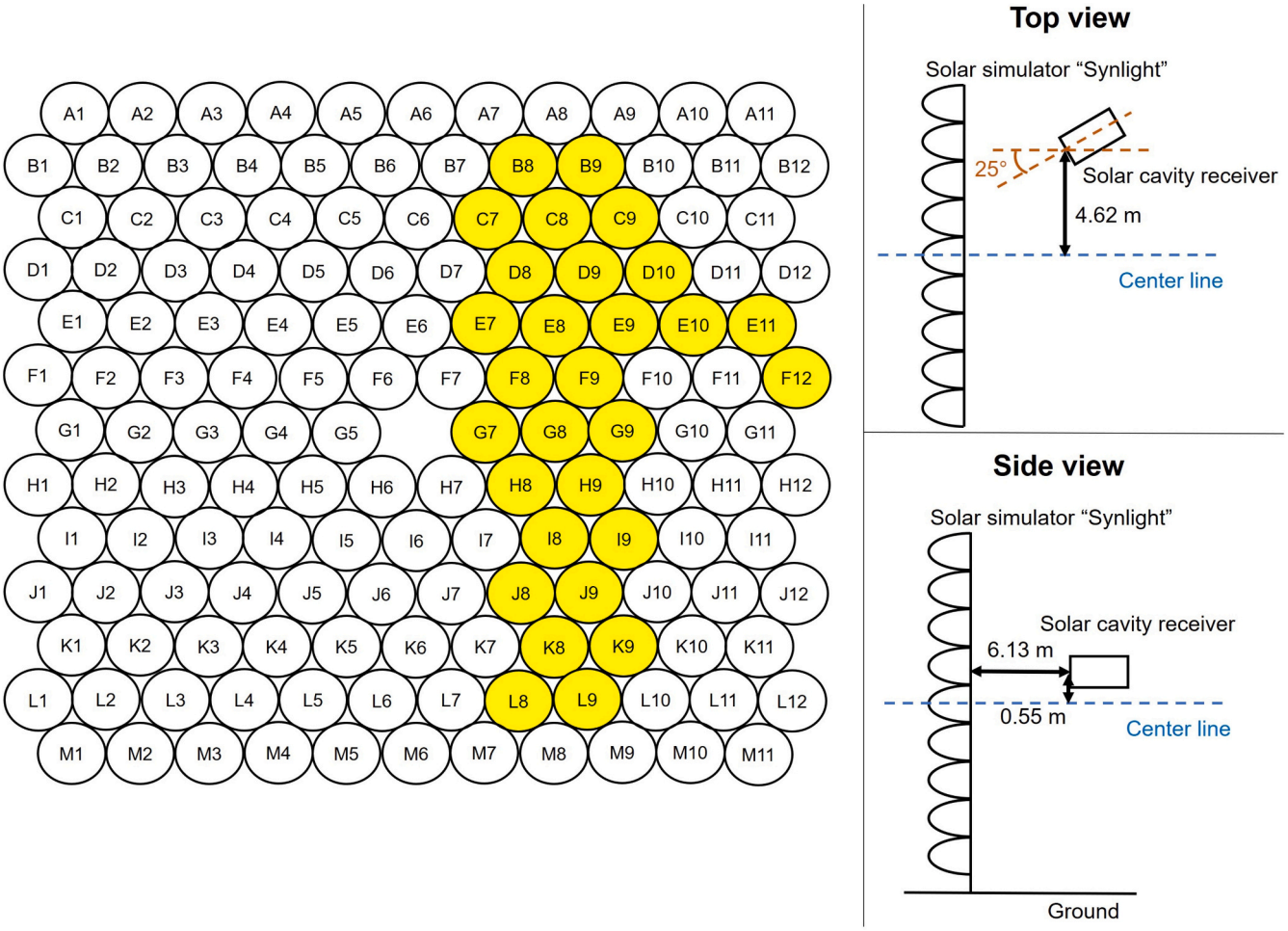


**Fig. 3.** "Synlight" lamps' location and receiver position.

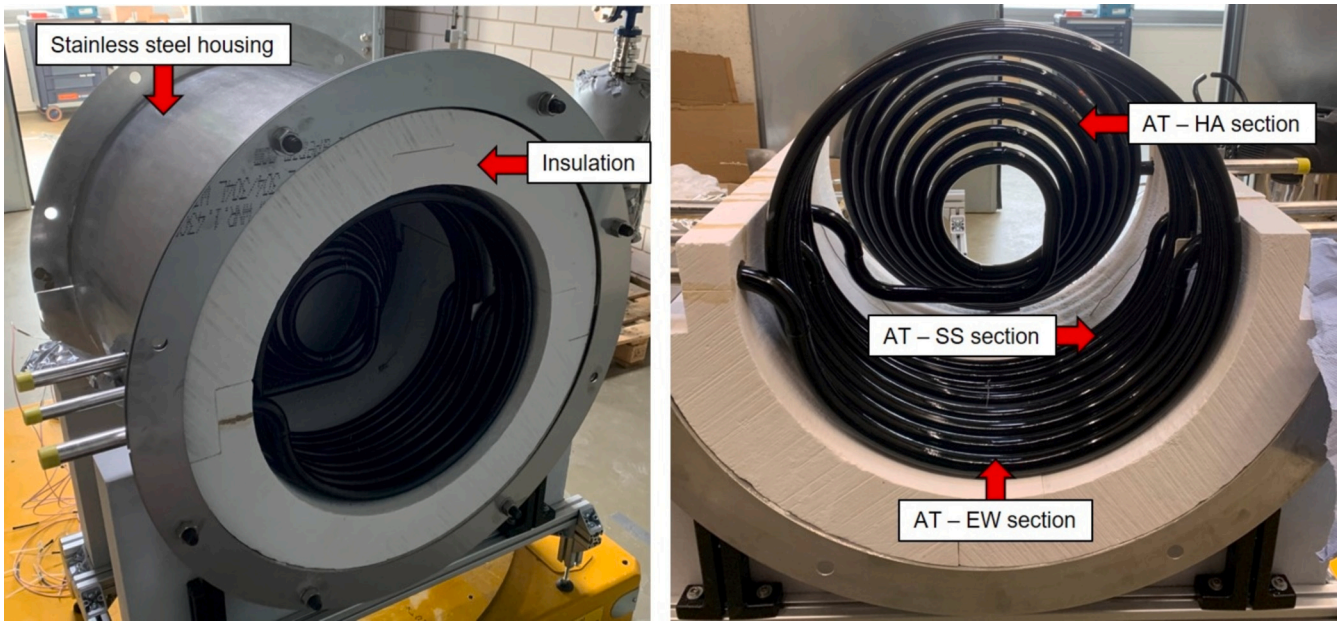


**Fig. 4.** Experimental design of solar cavity receiver.

efficiently absorb the irradiation of the lamps.

Table 1 shows the specifications of developed solar cavity receiver. The final design of cavity receiver and the parameters shown here were determined based on our numerical study and practical perspectives. The meaning of each parameter shown in Table 1 can also be confirmed from our previous paper [28]. Compared to the previous receiver design in the numerical study, the tube length for EW and SS sections and HA section were increased around 25 % and 5 %, respectively. This change was made to avoid any hot spots during the experiment. Furthermore, the larger increase rate in tube length in the EW and SS sections is in order to cover more surface area in the cavity by AT.

**Table 1**
Specifications of developed solar cavity receiver.

| Specifications | | Values |
|---|---|---|
| AT for EW section | Inner diameter | 0.019 m |
| | Outer diameter | 0.025 m |
| | Length | 5.51 m |
| | Projected diameter for winding | 0.50 m |
| | Winding number | 3.5 |
| | Pitch | 0.028 m |
| AT for SS section | Inner diameter | 0.014 m |
| | Outer diameter | 0.020 m |
| | Length | 5.49 m |
| | Projected diameter for winding | 0.495 m |
| | Winding number | 3.5 |
| | Pitch | 0.023 m |
| AT for HA section | Inner diameter | 0.019 m |
| | Outer diameter | 0.025 m |
| | Length | 7.91 m |
| | Projected diameter for winding | 0.20–0.50 m |
| | Winding number | 7.0 |
| | Pitch | 0.030 m |
| | Taper angle | 40° |
| Cavity insulation, side | Aperture's inner diameter | 0.545 m |
| | Aperture's outer diameter | 0.745 m |
| | Length | 0.574 m |
| Cavity insulation, back | Diameter | 0.745 m |
| | Thickness | 0.050 m |
| AT, surface emissivity | | 0.95 |
| Cavity insulation, solar reflectivity | | 0.87 |
| Cavity insulation, emissivity in near infrared region | | 0.26 |
| Receiver horizontal angle | | 25° |

The surface emissivity value of the black paint on AT is provided from Helling GmbH [36]. The cavity insulation's solar reflectivity and emissivity in near infrared region were measured at ambient temperature by "Lambda 950 UV/Vis/NIR spectrophotometer". Although these values may vary at high temperatures, they were used in our numerical analysis because our previous studies have demonstrated that these factors do not significantly affect receiver performance. The receiver horizontal angle indicates how horizontally the receiver is tilted with respect to the solar simulator as shown in Fig. 3. In other words, 0° of receiver horizontal angle indicates that the receiver faces the solar simulator.

### 2.4. Thermocouples' location on the cavity receiver

Multiple type N thermocouples were attached inside and outside of the cavity receiver to investigate the temperature behavior. Fig. 5 describes the thermocouples' location on the cavity receiver.

As shown in the figure, 14 thermocouples (TR 1–14) and 6 thermocouples (TR 15–20) were used inside and outside of the cavity receiver, respectively. TR 1–4 were placed on the cavity side wall near the receiver opening. TR 5–8 (inside) and TR 15–18 (outside) were installed on the middle area of cavity side wall. TR 9–12 were mounted in the rear area of the cavity side wall. TR 13–14 (inside) and TR 19–20 (outside) were placed on the cavity back wall. The detailed location of each thermocouple can be seen in the figure.

### 2.5. Uncertainty analysis

The uncertainty analysis was conducted as with our previous study [27] with the following assumptions.

- Random error is the predominant error of the experimental devices.
- The errors follow a normal distribution.

The uncertainties in temperature, pressure, mass flow, solar flux measurements and other data acquisition devices were calculated.

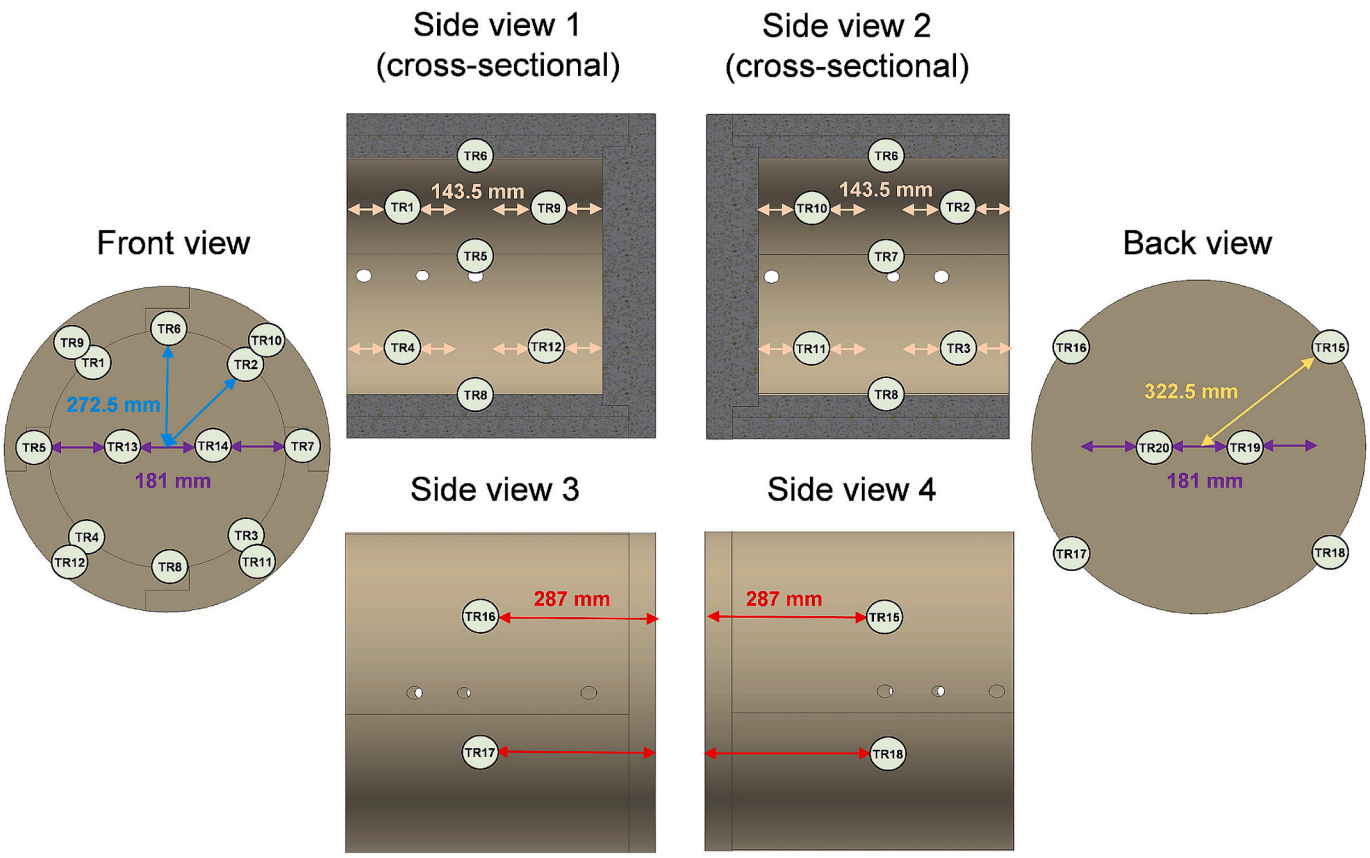


**Fig. 5.** Thermocouple's location on the cavity receiver.

Furthermore, the uncertainty of solar cavity receiver's energy efficiency was calculated based on those uncertainties. The experimental devices' accuracy and ranges are shown in Table 2.

## 3. Heat flux measurement and simulation

This section first represents the measured and simulated 2D heat flux map of solar simulator "Synlight" at the receiver aperture, followed by the simulated 3D heat flux map inside the cavity receiver. The measurement of the 2D heat flux map was conducted by using the optical measurement system FMAS (Flux Mapping Acquisition System) [37]. The simulation of 2D and 3D heat flux maps was performed with FEMRAY (Finite Element Mesh Ray Tracing) approach. This approach is explained in more detail in our previous study [28]. The position of the lamps in the simulation was manually adjusted to the solar simulator's recorded position to account for possible uncertainties.

**Table 2**
Experimental devices' accuracy and ranges. Where |t|, (a), Rd, and FS indicate the actual temperature in °C, absolute value, reading and full scale, respectively.

| Experimental devices | Accuracy | Range |
|---|---|---|
| Pressure transmitter | ±0.40 % FS | 0–400 kPa (a) |
| Thermocouple (type N) | ±0.004\|t\| | 0–1100 °C |
| Mass flow controller (EW section) | ±0.20 % Rd | 0–30 kg/h |
| Mass flow meter (SS section) | ±0.75–0.80 % Rd | 0–25 kg/h |
| Mass flow controller (HA section) | ±1.80 % FS | 0–85 kg/h |
| AD converter / Pressure transmitter module | ±0.76 % Rd | |
| AD converter / Thermocouple module | ±2.33 °C | |
| Solar simulator (one lamp) | ±3.0 % Rd [37] | 2.5–2.7 $kW_{rad}$ [38,39] |

### 3.1. 2D heat flux map at the receiver aperture

Fig. 6 shows the measured and simulated 2D heat flux distribution at the receiver aperture. The total radiation power applied to the receiver aperture was 71.0 $kW_{rad}$ with 29 lamps and intercept factor of 0.94. In other words, the total radiation power from the lamps were around 75.5 $kW_{rad}$.

In general, simulation and measurement show a similar shape of the flux density distribution and have the same average flux density. It can be observed from both maps that most of the lights from the lamps are concentrated in the center of the lower part of the aperture area (at a position of [−0.05 m, −0.1 m]). However, the simulation shows locally a higher flux density value than the measurement. The maximum flux density values for the simulation and measurement are 723.5 $kW_{rad}/m^2$ and 603.9 $kW_{rad}/m^2$, respectively. In addition, the range of low heat flux densities (below 200 $kW_{rad}/m^2$) in the measurement is greater than in the simulation. In other words, the low heat flux is more widely distributed in the measurement results than in the simulation results. Finally, the locations of the hot spots differ between the measurement results and the simulation results. For example, two small circular hotspots can be observed in the simulation results (at positions of [−0.15 m, 0.0 m] and [−0.03 m, −0.1 m]), while only one large triangular hotspot can be observed in the measurement results (at a position of [−0.05 m, −0.1 m]).

The main reason for the difference in heat flux density values can be explained by the different outputs of the lamps used and the non-ideal flux map (i.e. no gaussian distribution). It can be considered that the performance of the lamps used in the experiment had deteriorated over time, and not all of the lamps used had the same performance. Moreover, the difference in the flux map of a single lamp is also thought to have caused the difference. It is expected that the actual lamp used had a lower peak heat flux and a wider range of low heat flux density than the

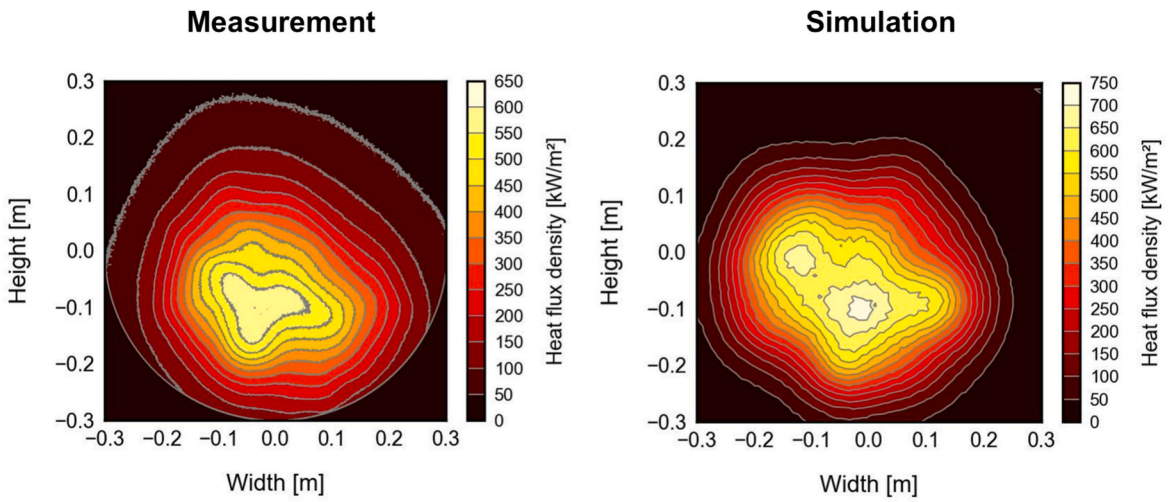


**Fig. 6.** Measured and simulated 2D heat flux map at the receiver aperture.

simulated or ideal heat flux. The main reason for the difference in the location of the hotspot can be explained by the positioning uncertainties of the lamps. Since the position of the lamps in the simulation was manually adjusted, there were some errors and differences from the experiment, and this may have led to differences in the position of the hot spot.

### 3.2. 3D heat flux map inside the cavity receiver

Fig. 7 shows the simulated 3D heat flux distribution inside the cavity receiver.

As shown in the figure, the heat flux provided from solar simulator is most concentrated on the ATs, especially on the AT for HA section. This is because air required much more energy than water or steam in the other sections (the mass flow rate of air was set to four times that of water or steam). There are some parts that AT has comparativly low flux (e.g., the HA inlet part and EW and SS sections at the left, and due to the insulation and cavity design the outside of the tubes). Although the lamps were adjusted to provide a relatively uniform heat flux distribution in the AT, it was difficult due to the position of the lamps and receiver. As explained in Section 2.2, the cavity receiver was installed at the end of the solar simulator "Synlight" facility, so it was difficult to concentrate light on every part of the AT (especially the left side of the cavity receiver). However, it was relatively easier to avoid the concentration of light on the cavity inner wall as shown in the figure. Based on the shown heat flux distribution, the receiver's performance such as fluid temperature at EW, SS, and HA sections, cavity inner wall temperature, and cavity outer wall temperature were calculated using the coupled 1D—3D numerical model built in our previous study [27,28].

## 4. Results and discussions

This section first presents the overall experimental results, including experiments at nominal and low power, followed by the validation results by using the quasi steady-state data, the parameter studies, and finally the efficiency comparison with existing literature.

### 4.1. Experiment with nominal power

The proposed receiver concept with 70 $kW_{th}$ nominal power was built and tested for 4 days (around 20 h in total) by using the DLR solar simulator "Synlight" [30,39]. During consecutive test periods, the solar cavity receiver operated without failure, except for the absorptive coating on the AT. Some of the coating peeled off after several tests. Nevertheless, the proposed receiver concept was able to produce hot steam and air at the target temperature on all test days.

#### 4.1.1. Fluid behavior inside AT

Fig. 8 shows the experimental results of fluid behavior in each AT section. Outlet temperature, outlet pressure, mass flow rate of air and

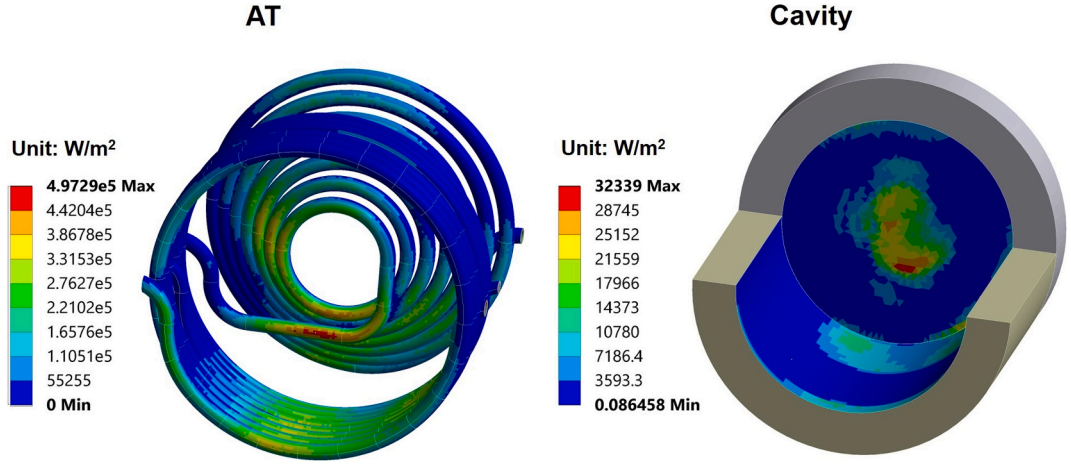


**Fig. 7.** Simulated 3D heat flux map inside the cavity receiver.

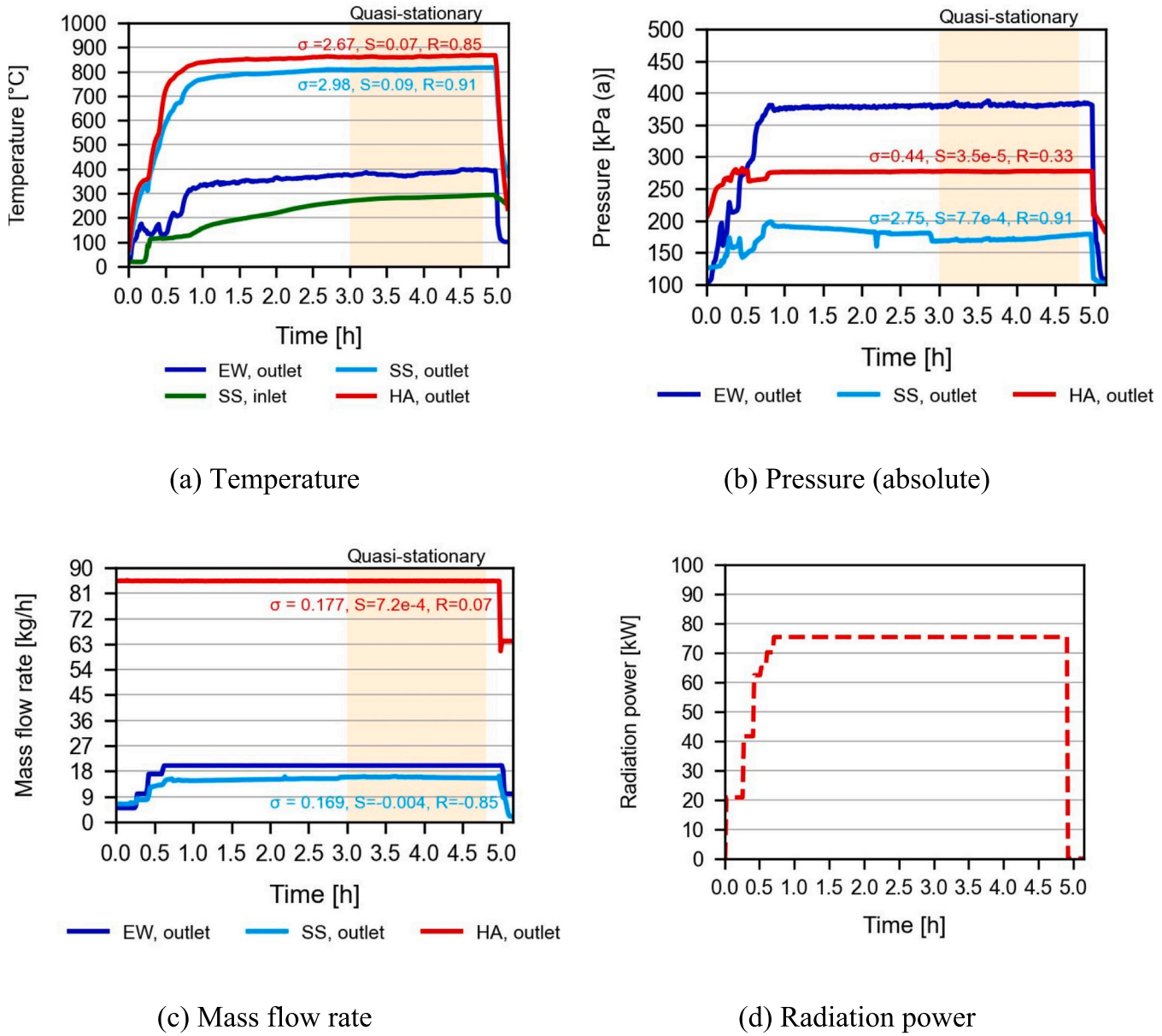


**Fig. 8.** Experimental results of fluid behavior in each AT section – Nominal power.

steam coming out from each AT section are depicted. Moreover, the radiation power of solar simulator "Synlight" is shown in one separate figure to represent the applied power over time. The steam inlet temperature, as varied over time by the steam accumulator, is also shown in the temperature graph. Finally, the standard deviation (σ), slope (S), and correlation coefficient (R) of the outlet temperature, outlet pressure, and mass flow rate of the heated steam and air in the SS and HA sections are added to the figures. These values were taken for experimental durations ranging from 3 to 4.8 h (quasi steady-state), as shown in the light orange background. The units for standard deviation and slope are the units of the y-axis and the units of the y-axis/min in each figure, respectively. The purpose of calculating the standard deviation, slope, and correlation coefficient is to clarify how stably the solar cavity receiver can generate hot steam and air in a quasi-steady state.

At the start of the experiment, the total lamp power is successfully increased in steps by adding lamps until all 29 lamps (75 $kW_{rad}$) are lit. The mass flow rate in the EW section is also increased in steps according to the lamp power in order to continuously generate steam and store it in the steam accumulator. The mass flow rate in the SS section follows a similar trend (stepwise increase) as in the EW section, while the mass flow rate in the HA section is kept constant. The outlet pressure is adjusted by the valves according to the mass flow rate (or velocity) of the fluid, not to exceed 400 kPa (a) in the EW section, 200 kPa (a) in the SS section, and 300 kPa (a) in the HA section. Here, note that the air is supplied for the first 0.25 h of the SS section. The mass flow rate (6 kg/h), inlet temperature (20 °C), and outlet pressure (130 kPa (a)) shown during this time is the value for the air flow. The system enters a quasi stationary phase approximately 1 h after initiation, and the experiment continues in this phase for about 4 h. At the end of the experiment, all lamps are turned off at once and the mass flow rate in the EW and HA sections are lowered to slowly cool down the system. The generated steam stored in the steam accumulator is discharged until there is no more steam from the vessel, as shown in the decrease in mass flow rate in the SS section of the figure. The drop in outlet pressure shown in the figure is due to the valve being fully opened.

In the quasi stationary phase, the mass flow rate is nearly constant in the EW (20 kg/h) and HA (85 kg/h) sections, but not in the SS section (15–16 kg/h). The outlet pressure in the EW, SS, and HA sections are

adjusted to 400 kPa (a), 200 kPa (a), and 300 kPa (a), respectively. After 2.2 h in the SS section, some peaks can be observed in the mass flow rate and the outlet pressure. The outlet temperature in the EW, SS, and HA sections stabilizes at around 385 °C, 811 °C, and 863 °C, respectively. The inlet steam temperature in the SS section becomes stable three hours after the start of the test.

The mass flow rates in the EW and HA sections were constant since the flows were controlled by mass flow controllers. On the other hand, the mass flow rate in the SS section was fluctuating due to the flow coming from the steam accumulator. Since the mass flow rate was controlled by adjusting the stream pressure (including the pressure inside the steam accumulator) with a valve, larger fluctuations in the mass flow rate were observed in the SS section compared to the other sections. The outlet pressure in the SS section became lower than the EW section due to the pressure drop inside the steam accumulator. The peaks seen in the mass flow rate and outlet pressure in the SS section are due to changes in operating mode. ON and OFF of the needle valves (NVA-2 and NVA-3 in Fig. 1) were switched 2.2 h after the start of the test, and the high-temperature steam started flowing into the TES. This switchover resulted in a rapid decrease in steam pressure and a rapid increase in mass flow rate. However, these peaks were observed only in a short period. The slow rise in the inlet steam temperature is due to the slow response of the steam accumulator. In other words, the steam accumulator took longer to reach a steady state. The solar simulator lamps were turned on in stages at the beginning to avoid rapid heating, which could cause thermal shock to ATs [40].

The designed solar cavity receiver could simultaneously produce high-temperature steam (811 °C) and air (863 °C). These results were reproducable in two other experiments (Appendix B). The air and steam temperatures obtained and the relatively low standard deviations and slope values shown in Fig. 8 imply that the combination of CST and HTE is promising as heat can be supplied continuously and steadily.

#### 4.1.2. Cavity temperature

Fig. 9 shows the experimental results of cavity inner and outer temperature. The location of TR 1–20 can be seen in Section 2.4. Here, the average temperatures at each section (TR 1–4: cavity inner side wall near to receiver aperture, TR 5–8: cavity inner side wall on the middle area, TR 9–12: cavity inner side wall in the rear area, and TR 13–14: cavity inner back wall) are shown in Fig. 9 (a). Furthermore, in Fig. 9 (a), the graph has been expanded in the range of 0 to 0.5 h (x-axis) and 0 to 650 °C (y-axis) in order to more clearly observe the temperature change. The other two experimental results of cavity temperature are shown in Appendix B.

In general, the temperatures of the inner cavity have a similar profile as the AT's temperatures. The cavity inner temperature reacts quickly at the start and end of the experiment in accordance with the lamp's output (as shown in Fig. 8 (d)). At the start of the experiment (after 0.25 h), the temperature inside the cavity drops momentarily. However, the temperature continues to rise, and it stabilizes when all 29 lamps light up (after 0.8 h). The cavity outer temperature has much slower response compared to the cavity inner temperature. After about 4.5 h, the temperature reaches a quasi-steady state. The thermocouples close to the receiver aperture (TR 1–4) tend to have lower temperatures, while the thermocouples located on the middle or in the rear of the cavity inner side wall (TR 5–12) have higher temperatures. Furthermore, thermocouples mounted on the inside of the cavity back wall (TR 13–14) show almost the same temperature behavior as thermocouples mounted on the rear of the cavity inner side wall (TR 9–12). It can be observed that the thermocouples mounted on the upper part of the cavity outer wall (TR 15 and TR 16) have higher temperatures.

The cavity outer temperature had much slower response due to the insulation of the cavity wall. The cavity inner temperature had a quick response since the cavity inner surface was initially heated or cooled. In other words, the thermocouples inside the cavity promptly detected a rise in temperature when the lamp was turned on, and a fall in temperature when the lamp was turned off (at this moment, the fluid was flowing in each tube). The instantaneous drop in the temperature of inner cavity after 0.25 h was due to the change in the fluid in the SS section from air to saturated steam. As a result of the above change, the AT temperature in the SS section has decreased (due to the latent heat of water evaporation), and the cavity inner temperature has decreased. The thermocouples TR 1–4 had lower temperatures than the other locations due to the greater influence of natural convection and radiation caused by the opening aperture. Furthermore, the low AT temperature in the EW section due to water evaporation was another reason for the lower temperatures of thermocouples TR 1–4. The thermocouples TR 13–14 and TR 9–12 showed a similar temperature behavior since they were placed in close proximity and the heat loss rate in the rear region of the cavity inner wall was very low. The thermocouples TR 15 and TR 16 had higher temperatures compared to the other thermocouples (TR 17–20) due to the natural convection effect. It is considered that the upper part of cavity inner wall was heated more by the hot air rising due to natural convection, and more heat was transferred to the upper part of cavity

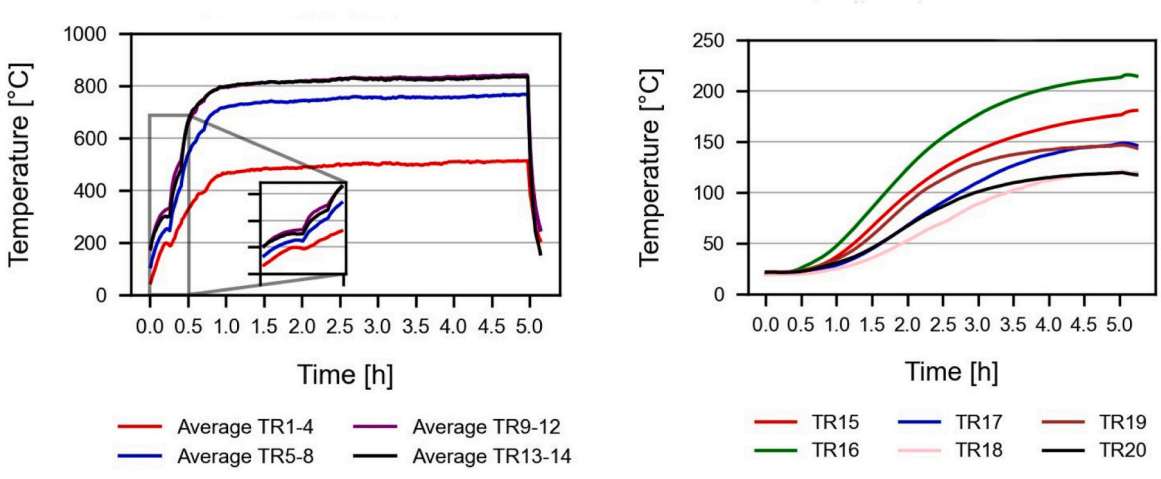


(a) Cavity inner temperature (b) Cavity outer temperature

**Fig. 9.** Experimental results of cavity temperature.

outer wall through thermal conduction.

As the results show, cavity insulation contributed to efficient heat transfer to the working fluid by reducing thermal conduction losses from the receiver and keeping the temperature inside the cavity high.

### 4.2. Experiment with low power

The proposed receiver concept with 70 $kW_{th}$ nominal power was also tested with low power. In other words, the receiver concept was tested with less fluid mass flow rate and less radiation power. Fig. 10 shows the experimental results of fluid behavior in each AT section. As with Fig. 8, outlet temperature, outlet pressure, and mass flow rate of air and steam coming out from each AT section, steam inlet temperature, and radiation power of solar simulator are depicted.

The radiation power starts from 20.8 $kW_{rad}$. After 0.5 h, one lamp is turned on and the total lamp power is set to 23.4 $kW_{rad}$. The total power is kept at this value until 2.0 h, after which three additional lamps are turned on in stages up to 31.2 $kW_{rad}$ until 2.6 h. These additional lamps mostly irradiated the HA section. After 2.6 h, four lamps are turned on for the EW and SS sections, and the total power becomes 41.6 $kW_{rad}$. After 2.8 h, one additional lamp is tunred on for the SS section, while the other lamp is turned off after 2.9 h. After 3.3 h, one lamp for HA section is turned on to further heat the air. After 3.6 h, all lamps are turned off and the experiment is terminated.

In the EW section, the water mass flow rate is set to 5 kg/h at the start. The outlet temperature remains at boiling temperature of water until 0.5 h. In other words, the water is not completely evaporated at this point. After 0.5 h, the EW section begins to produce superheated steam due to increased radiation power. This section is providing the superheated steam at approximately 300 °C until 2.0 h. After 2.0 h, the outlet temperature of the EW section gradually increases with increasing radiation power (less than 400 °C). This power increase was mainly for the HA section, but the EW section was also affected. The mass flow rate is increased to 10 kg/h after 2.6 h, and this value is maintained until the end of the experiment. The outlet temperature increases even with increasing mass flow rate due to increased radiation power in the EW and SS sections. The outlet pressure in the EW section increases after 2.0 h by partly closing the valve in the SS section (NVA-2 in Fig. 1). A decrease in outlet temperature and pressure can be observed after all lamps are turned off. During the experimental period, the outlet temperature varies widely.

In the SS section, the air is supplied for the first 0.5 h. The mass flow rate (6 kg/h), inlet temperature (23 °C), and outlet pressure (160 kPa (a)) shown during this time is the value for the air flow. After 0.5 h, the valves (SV and BVA) switch and steam stored in the steam accumulator begins to flow into the SS section. This change can be observed in a decrease in outlet temperature, outlet pressure, and mass flow rate and an increase in inlet temperature. Until 2.0 h, the saturated steam at 100 °C and ambient pressure is provided to this section from the steam accumulator. The mass flow rate and the outlet temperature are fluctuating in the range of 5–6 kg/h and 400–500 °C, respectively. After 2.0 h, the outlet pressure increases and the mass flow rate decreases by closing the valve (NVA-2). The outlet temperature begins to gradually increase with increasing irradiation power (most of the irradiation

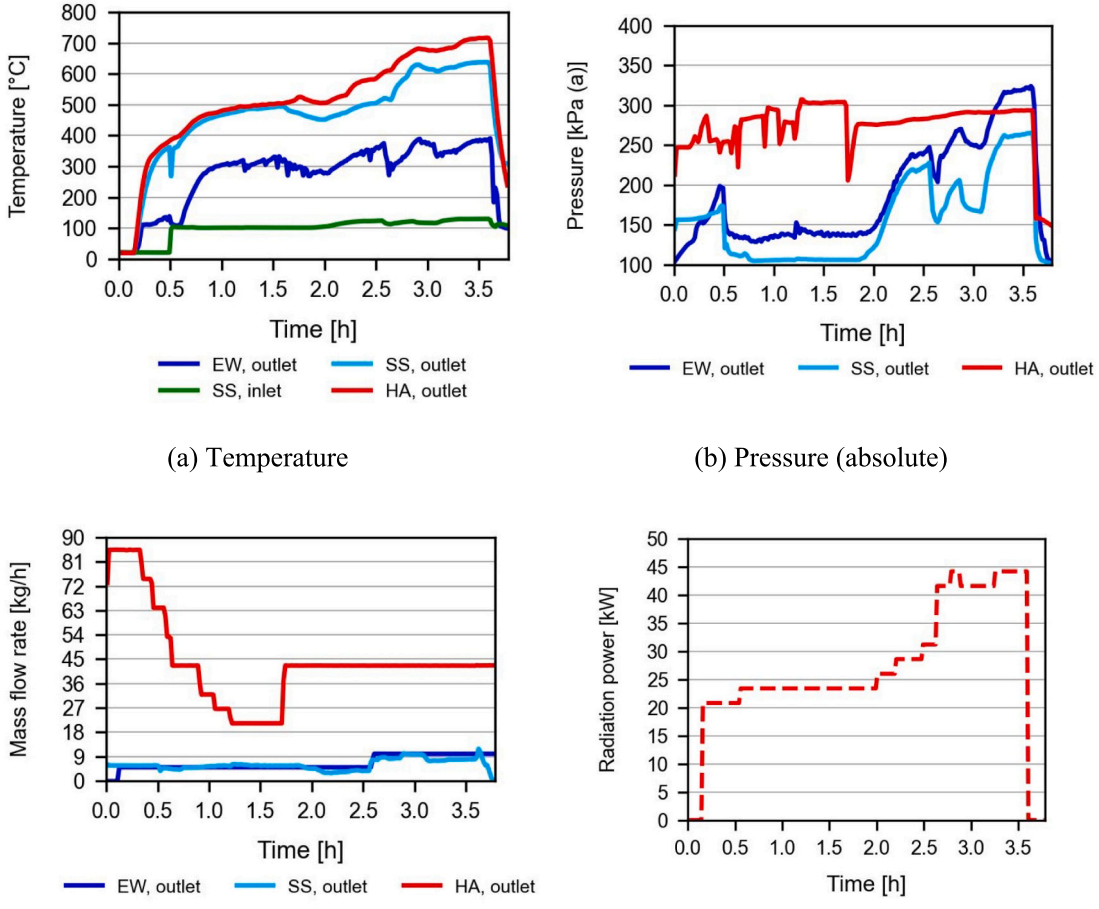


**Fig. 10.** Experimental results of fluid behavior in each AT section – Low power.

power was concentrated in the HA section, but some was also irradiated in the SS section). After 2.5 h, the outlet pressure decreases and the mass flow rate increases by partly opening the valve (NVA-2). Although there are fluctuations, the outlet temperature also rises to around 600 °C due to increased radiation power in the EW and SS sections. The mass flow rate fluctuates after 2.6 h due to pressure fluctuations, but stabilizes at about 8 kg/h at the outlet pressure of 260 kPa (a) at the end of the experiment. After 3.6 h, the mass flow rate suddenly increases and then drops. A decrease in outlet temperature and pressure can be observed after all lamps are turned off.

In the HA section, the starting air mass flow rate is set at 85 kg/h and lowered in steps to 21 kg/h until 1.2 h. The outlet pressure is fluctuating, but is adjusted to near 300 kPa (a). The outlet temperature is rising to 500 °C. For 1.2 to 1.6 h, the mass flow rate, outlet temperature, and outlet pressure are stable at 21 kg/h, 500 °C, and 300 kPa (a). After 1.6 h, the mass flow rate increases to 43 kg/h and remains fixed until the end of the experiment. The outlet pressure is adjusted by the valve (NVA-1) to maintain the value less than 300 kPa (a). The outlet temperature increases with increasing radiation power, reaching 700 °C. A decrease in outlet temperature and pressure can be observed after all lamps are turned off.

One lamp was turned on after 0.5 h to produce the superheated steam in the EW section. The air was flowing in the SS section for the first 0.5 h because there was not enough steam in the steam accumulator. The air mass flow rate in the HA section was gradually decreased until 1.2 h from the start to avoid overheating of the AT. During this period, the outlet pressure fluctuated due to changes in the mass flow rate. The air mass flow rate was increased after 1.6 h to further heat the air without any overheating. The water mass flow rate in the EW section was increased to 10 kg/h after 2.6 h to avoid heating the exiting steam above 400 °C. Temperatures in the EW section were kept lower than that because temperatures above 400 °C could melt the sealing of the piping. This increase in mass flow rate in the EW section also caused an increase in mass flow rate in the SS section. One lamp was turned on after 2.8 h, but turned off immediately after 2.9 h for the same reason as the increase in mass flow rate in the EW section. The outlet temperature in the SS section from 2.7 to 3.1 h were variable because the lamps were on and off. The sudden increase in the mass flow rate in the SS section after 3.6 h was due to the valve being fully opened (NVA-2). The steam stored in the steam accumulator was discharged at once, resulting in a rapid increase in mass flow rate. The outlet pressure in all sections decreased after all lamps were turned off since the valves (NVA-1 and NVA-2) were fully opened.

In summary, the solar receiver with low power could not produce high-temperature air and steam hotter than 800 °C. One of the main reasons is that the SS section had a much lower inlet temperature. In other words, the mass flow rate of the steam was so low that the steam accumulator could not reach steady state and provide superheated steam during this experimental time. This steam accumulator behavior also caused erratic operation in the EW and SS sections. Similar behavior of steam accumulators at low steam mass flow rates (5 kg/h) was also observed in Schiller's study [9]. A lower inlet steam temperature resulted in a lower outlet steam temperature in the SS section. In addition, due to larger temperature gradient and re-radiation phenomena, more heat was transferred from the HA section to the SS section, resulting in lower outlet air temperatures. The extra lamps for air heating were not added to account for reduced heat transfer coefficient and overheating of the tubes. In other words, the additional lamps were not lit for air heating so that the temperature of the tube wall would not exceed 1050 °C (maximum operating temperature of high-temperature stainless steel 1.4841 [41]). Because the solar receiver and steam accumulator were designed on a larger scale, the designed system could not produce hot fluid at the target temperature with a low power. However, the system was able to supply hot steam at 600 °C and hot air at 700 °C.

### 4.3. Validation

This section shows the comparison results between the experiment and simulation. Firstly, the outlet temperature of air and steam coming out from each AT section is shown, followed by the outlet pressure, and finally the lamp-to-thermal efficiency. The quasi steady-state data of the experiment are used as inlet conditions for the numerical simulation and are shown in Table 3. And those data for other two experiments (including the validation results) are shown in Appendix C. The average ambient temperature during the test was 27.8 °C.

Fig. 11 shows the comparison results of the outlet fluid temperatures. The experimental results are shown in the left bar with black dots, while the numerical results are shown in the right bar with diagonal lines. The orange line is an error bar indicating the uncertainty due to the measurement.

The errors between experiment and simulation for EW, SS, and HA sections are 8.97 %, 0.60 %, and 0.78 %, respectively. The errors for EW section became larger than the other sections due to the effects of complex boiling flow phenomena [42]. It can be considered that the numerical model used for single phase flow is suitable, while the 1D—3D numerical model used for two-phase flow needs further improvement, which may have made a difference in the results. However, the error is less than 10 %, a relatively good prediction given the simpler model used in this study.

Fig. 12 shows the comparison results of the outlet fluid pressures.

The experimental results agree well with the simulation results in EW (4.26 % error) and HA (4.20 % error) sections. There is a fairly large error in the SS section (20.10 % error), but it is smaller on the other two experimental dates (6.71 % and 7.37 % error), as shown in Appendix C. This leads to the consideration that some error occurred during the test (e.g., an offset in the valve position), resulting in a larger error only on this experimental day. The numerical model underestimates the pressure losses in EW and SS sections, while it overestimates the pressure losses in HA section. The underestimation in the EW and SS sections may be due to the roughening of the tube surface by oxidation. Since the numerical model considers smooth surface for the pressure loss calculation, and the hot water or steam is more corrosive against the stainless steel compared to the dry air [43,44], a fast oxidation may have occurred in the inner tube surface and resulted in the underestimation. The overestimation in the HA section may be due to the difference in the heat flux distribution on the AT between the experiment and the simulation. In other words, in the simulation, the air was heated over a shorter distance than in the experiment, and the hotter (or lower density) air flowed through the tube over a longer distance, resulting in a greater pressure drop. However, it can be concluded that the errors shown are relatively small (less than 10 %).

Fig. 13 shows the comparison results of lamp-to-thermal efficiency. It is the efficiency of energy transferred from the lamp as light to the inside of the cavity receiver as heat. Note that the electricity consumption of the lamps is not considered in this efficiency. Further explanation and the equations can be seen in our previous study [28].

As the figure shows, the numerical results are within the uncertainty range of the experimental results. The difference between experiment and simulation is 0.28 %. Similar results were obtained in the other two experimental days as shown in the Appendix C.

In this section, it was demonstrated that the developed numerical model can predict the solar cavity receiver's behavior (outlet fluid

**Table 3**
Quasi steady-state data (experimental durations ranging from 3 to 4.8 h) of experiment used as inlet conditions for the numerical simulation.

| AT section | Inlet temperature | Inlet pressure | Mass flow rate |
|---|---|---|---|
| EW | 27.2 °C | 398.2 kPa (a) | 20.0 kg/h |
| SS | 282.7 °C | 216.3 kPa (a) | 15.8 kg/h |
| HA | 20.2 °C | 307.3 kPa (a) | 85.3 kg/h |

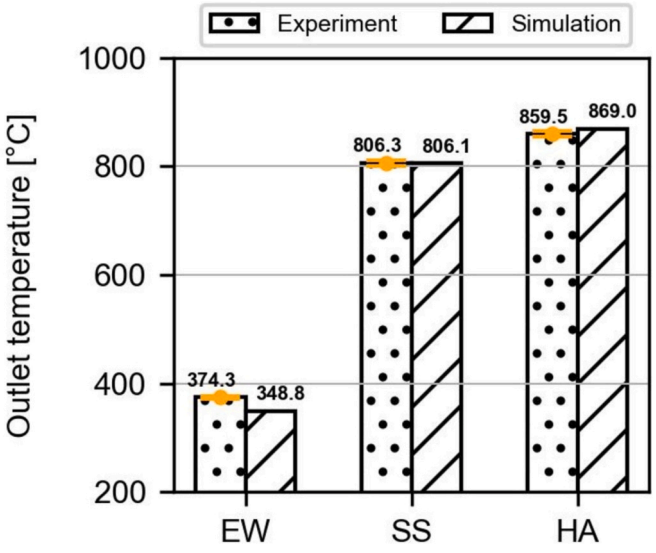


**Fig. 11.** Comparison results of outlet fluid temperature.

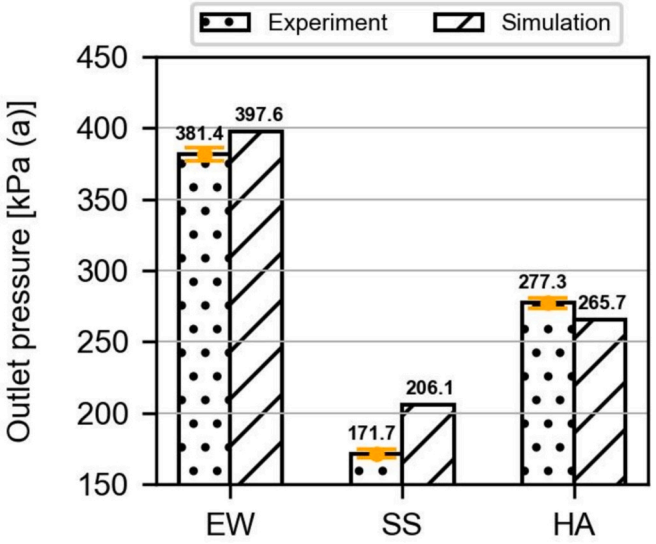


**Fig. 12.** Comparison results of outlet fluid pressure (absolute).

temperature, outlet fluid pressure, and lamp-to-thermal efficiency) fairly well (less than 10 % error between experiment and simulation). The next section presents a parameter study of the numerical model to further examine the impact of uncertain parameters on the system.

### 4.4. Parameter study

This section shows the parameter study of the numerical model. Four different parameters, (a) power of individual lamps, (b) convective heat transfer coefficient inside the cavity, (c) receiver horizontal angle, and (d) absorptivity of ATs, were investigated. These four parameters were chosen because they were considered to have the highest impact on the receiver performances. Table 4 shows the range of parameter investigated.

Fig. 14 shows the parameter study results of power of individual lamps. The outlet fluid temperature is used as a result, as it is greatly affected by each parameter. The result range of the parameter variations is indicated by a green error bar. The numerical results (right bar with diagonal lines) are compared with the experimental results (left bar with black dots) to show the effect of each parameter on real data.

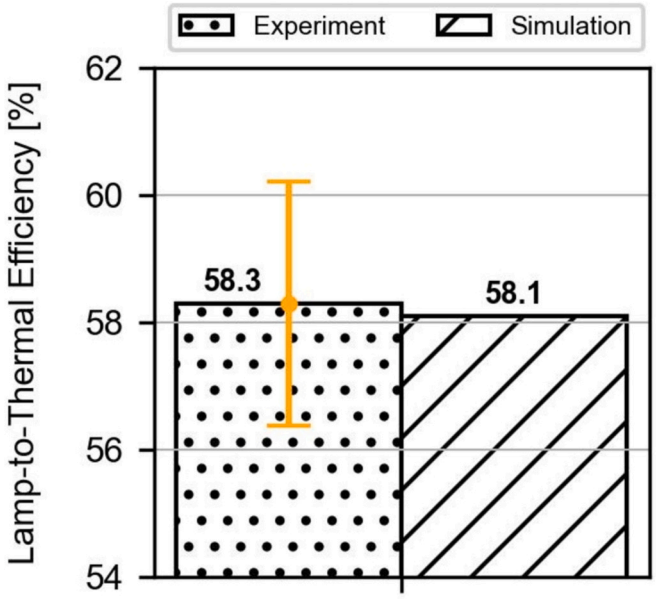


**Fig. 13.** Comparison results of lamp-to-thermal efficiency.

**Table 4**
Parameter range.

| Parameter | Range | Unit |
|---|---|---|
| Power of individual lamps | 2.5–2.7 | $kW_{rad}$ |
| Convective heat transfer coefficient inside the cavity | 7.57–15 | $W/m^2$ K |
| Receiver horizontal angle | 20–30 | ° |
| Absorptivity of ATs | 0.56–0.95 | |

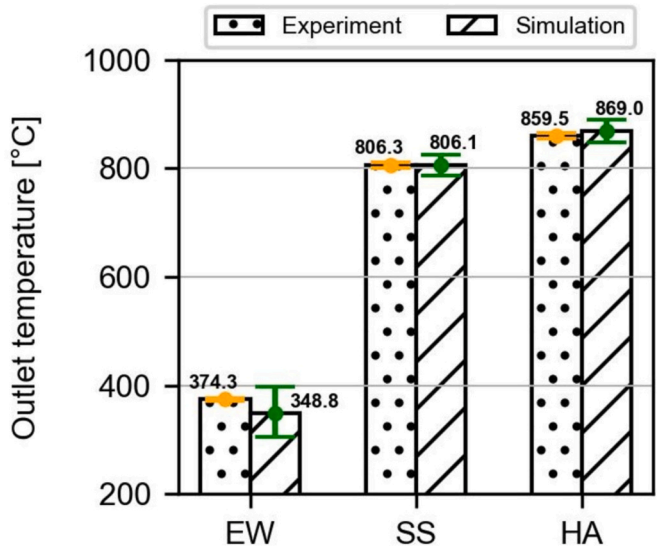


**Fig. 14.** Parameter study results (outlet fluid temperature) - Power of individual lamps.

Three different individual lamp powers, (1) 2.5 $kW_{rad}$, (2) 2.6 $kW_{rad}$, and (3) 2.7 $kW_{rad}$, were selected, and the numerical simulation was performed based on these three values to investigate their effects. The power of 2.6 $kW_{rad}$ is the base case and the values shown in the figure (simulation side) are the results of using this base case power. Note here that only the total power applied to the receiver changes, while the heat flux distribution in the cavity remains the same. The range of the individual lamp powers was chosen based on the accuracy of the lamps [37]

and the previous studies [38,39]. The lower limit of the green error bar (EW: 305.4 °C, SS: 786.2 °C, HA: 848.3 °C) shows the results when the individual lamp powers of 2.5 $kW_{rad}$ is used. On the other hand, the upper limit of the green error bar (EW: 397.0 °C, SS: 824.9 °C, HA: 889.1 °C) shows the results when the individual lamp powers of 2.7 $kW_{rad}$ is used. It can be observed that the individual lamp powers have great effect on the outlet fluid temperatures. Since the experimental values are within the range of the green error bars, it is indicated that the individual lamp powers of the solar simulator are in this range and uncertainty in the lamp power could be one reason for the deviations.

Fig. 15 shows the parameter study results of convective heat transfer coefficient inside the cavity.

Three different convective heat transfer coefficients, (1) 7.57 W/$m^2$ K, (2) 10 W/$m^2$ K, and (3) 15 W/$m^2$ K, were selected, and the numerical simulation was performed based on these three values to investigate their effects. The heat transfer coefficient value of 7.57 W/$m^2$ K is the base case and it was calculated based on an empirical equation (which is explained in our previous study [27]). The values shown in the figure (simulation side) are the results of using this base case heat transfer coefficient. Higher heat transfer coefficient values were considered since the ventilation system was operated during the experiment. The lower limit of the green error bar (EW: 254.3 °C, SS: 725.2 °C, HA: 781.2 °C) shows the results when the convective heat transfer coefficient of 15 W/$m^2$ K is used, while the upper limit of the green error bar shows the base case results. It can be seen from the figure that higher heat transfer coefficient values have a negative impact on the outlet fluid temperature. Since higher values of heat transfer coefficient result in a larger error compared to the experimental value, it can be considered that the ventilation system had a low effect during the experiment. This consideration is supported by the fact of large experimental room (floor area: 25.47 $m^2$, height: 5 m, performance of the ventilation system: 21444 $m^3$/h) and opening window that is connected to the lamp hall (air enters the experimental room through the opening window). Therefore, it is sufficient to consider only the effect of natural convection, and it can be concluded that the empirical equation used predicts that effect fairly well.

Fig. 16 shows the parameter study results of receiver horizontal angle.

Three different angles, (1) 20°, (2) 25°, and (3) 30°, were selected, and the numerical simulation was performed based on these three values to investigate their effects. The angle of 25° is the base case and the values shown in the figure (simulation side) are the results of using this base case angle. An angular error of 5° was considered in this study since a simple and manual measurement was conducted. The lower limit of the green error bar in EW (339.9 °C) and SS (799.3 °C) sections and the upper limit of the green error bar in HA section (879.4 °C) show the results when the angles of 20° is used. On the other hand, the upper limit in EW (374.8 °C) and SS (806.1 °C) sections and lower limit in HA section (856.5 °C) show the results when angles of 30° is used. The results in the figure indicate that the receiver horizontal angle has a small impact on the outlet fluid temperature. The reason for the different outlet temperature is due to the different heat flux distribution applied with the different receiver horizontal angle.

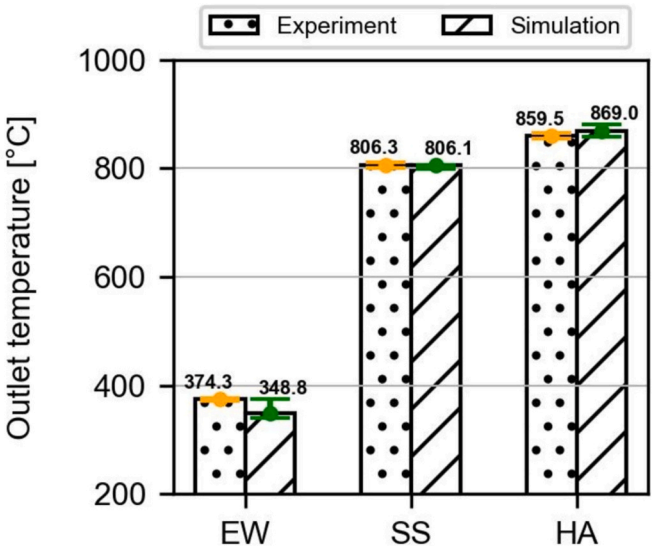


**Fig. 16.** Parameter study results (outlet fluid temperature) - Receiver horizontal angle.

Fig. 17 shows the parameter study results of absorptivity of ATs.

Three different absorptivities, (1) 0.56, (2) 0.76, and (3) 0.95, were selected, and the numerical simulation was performed based on these three values to investigate their effects. The absorptivity of 0.95 is the base case as explained in Section 2.2, and values shown in the figure (simulation side) are the results of using this base case absorptivity. The absorptivity of 0.56 is the minimum value for high-temperature stainless steel 1.4845, which is rolled [45]. The absorptivity of 0.76 is the average

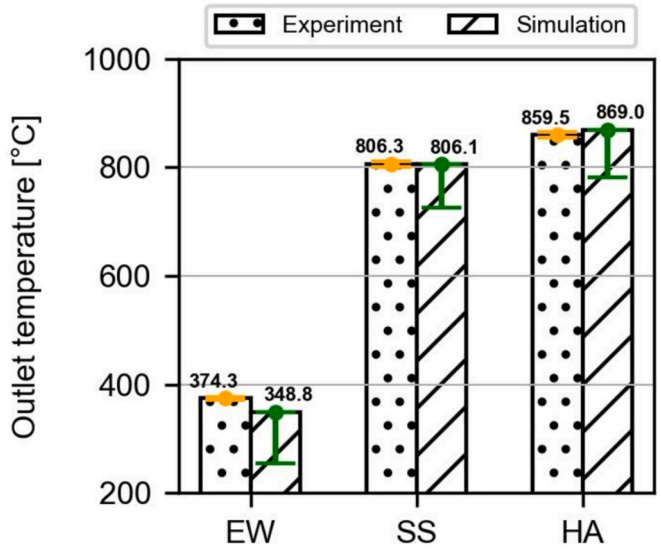


**Fig. 15.** Parameter study results (outlet fluid temperature) - Convective heat transfer coefficient inside the cavity.

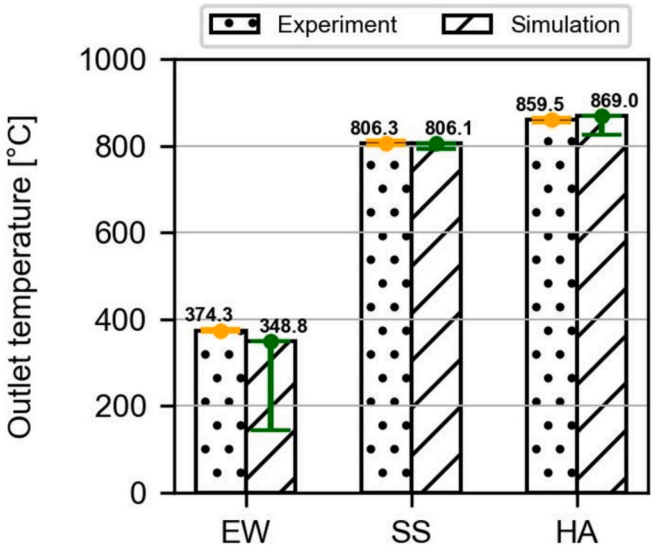


**Fig. 17.** Parameter study results (outlet fluid temperature) - Absorptivity of ATs.

value between 0.56 and 0.95. A lower absorptivity was considered because some of the black paint peeled off after several tests. The lower limit of the green error bar (EW: 143.4 °C, SS: 791.6 °C, HA: 824.7 °C) shows the results when the absorptivity of 0.56 is used, while the upper limit of the green error bar shows the base case results. It can be observed from the figure that the lower absorptivity have negative impact on the outlet fluid temperature. The results for the EW section are significantly influenced by absorptivity than for the other sections. This is because less irradiation energy is absorbed by the tube in the EW section and less energy is re-radiated to the EW section from the SS and HA tube sections that have much higher temperature. In the SS and HA sections, the irradiation energy absorbed by the tubes becomes lower with lower absorptivity, but the outlet fluid temperatures are not significantly affected due to the lower re-radiation. Since lower values of AT's absorptivity result in a larger error compared to the experimental value, it can be considered that the peeling of some black paint did not greatly affected the AT's absorptivity.

This section has demonstrated that the individual lamp powers, convective heat transfer coefficient, and AT's absorptivity have great effect on the outlet fluid temperatures at each AT section, while the receiver horizontal angle does not have much effect on that. In addition, from all results, it is observed that the impact of parameter variation is usually greatest in the EW section. This may be one of the reasons for the largest deviations between experimental and numerical results in the EW section of the base case. The overall results in this section also demonstrated that it is reasonable to use base case values for each parameter, despite the uncertainty in the parameters.

### 4.5. Efficiency comparison with existing literature

This section provides information on the efficiency of our receiver, as well as information on other receivers that have been developed and experimentally tested in previous studies. The receivers in the previous studies were selected based on four criteria: (1) uses cavity type, (2) uses absorber tubes, (3) produces high-temperature air or steam, and (4) has been experimentally tested. The receiver efficiency was redefined in all studies to fairly compared the values with each other. The definition of receiver efficiency is the ratio of the absorbed energy by the heat transfer fluid to the radiative power intercepted in the receiver aperture. The difference from our efficiency is that the spillage loss from the light source to the receiver aperture is not included in the input energy. Table 5 shows the comparative results of receiver efficiency. The radiative power intercepted in the receiver aperture and the achieved fluid temperature (including the type of fluid) are also shown in the table to indicate the scale and the product of receiver, respectively.

From the table, it is clear that the solar receiver concepts that have been tested most often are those on the scale of a few $kW_{th}$ (laboratory scale), and that there are only one receiver (except our study) that can produce both high-temperature steam and air. The comparative results indicate that the receiver efficiency of our study (64.3 %) is relatively higher than the efficiency of most of the past studies. This implies that our solar cavity receiver is a promising new concept that can provide both hot steam and air (more than 800 °C) compared to existing receiver concepts.

**Table 5**
Receiver efficiency comparison (asterisk mark indicates the efficiency calculated based on the data shown in the literature).

| | Radiative power intercepted ($kW_{th}$) | Achieved fluid temperature (°C) | Receiver efficiency (%) |
|---|---|---|---|
| Our study | 71.0 | 811 (steam)<br>863 (air) | 64.3 |
| Amsbeck et al. [46] | 272.8 | 803 (air) | 44.0 |
| Qiu et al. [24] | 1.8 | 570 (air) | 53.6 |
| Wang et al. [47] | 20–25 | 550 (air) | 60.0 |
| Zhu et al. [48] | 26.5 | 430 (air) | 80.0 |
| Chu et al. [25] | 7.4 | 787 (air) | 53.2 |
| Houaijia et al. [22] | 4.0 | 700 (steam) | 40.0 |
| Schiller et al. [9] or Kadohiro et al. [27] | 4.0 | 634 (steam) | 64.2* |
| Swanepoel et al. [49] | 1.7 | 343 (steam) | 50.0 |
| Lin et al. [26] | 0.91 | 700 (steam)<br>700 (nitrogen) | 32.0 |

## 5. Conclusion

A solar cavity receiver employing helical absorber tubes was experimentally investigated, and the obtained experimental results were compared with the numerical results. The 1D single and two-phase fluid flow model coupling with the 3D cavity heat transfer model, that was developed in our previous study, was used to numerically investigate the recever performances such as outlet fluid temperature, outlet fluid pressure, and lamp-to-thermal efficiency. The parameter studies were conducted to examine the impact of uncertain parameters on the receiver performances. Furthermore, the receiver efficiency of our study was compared with the existing literatures to investigate the effectiveness of the proposed solar cavity receiver concept. The key findings are:

- Experimental results at designed power have proven that the developed solar cavity receiver could successfully produce both the high-temperature steam (811 °C) and air (863 °C) with standard deviations of less than 3 °C (outlet temperature), 3 kPa (outlet pressure), and 0.2 kg/h (mass flow rate).
- Experimental results at partial load have demonstrated that the established solar cavity receiver was unable to produce hot steam and air at the target temperature and that the fluid flow was unstable due to the erratic operation of the steam accumulator. However, the system was able to supply hot steam at 600 °C and hot air at 700 °C. The control in partial load needs to be further investigated.
- Comparative study between the experiment and simulation have shown that the relative errors were less than 10 %, a relatively good prediction given the simpler model used in this study.
- Parameter studies have demonstrated that the individual lamp powers, convective heat transfer coefficient, and AT's absorptivity have great effect on the receiver performances. Furthermore, the effect of parameter variation was found to be greatest in the EW section compared to the other sections.
- Comparative results of receiver efficiency have indicated that our receiver concept is more efficient than most of the concepts of previous research. In other words, our solar cavity receiver is a promising new concept compared to existing receiver concepts.

The experimental study has demonstrated that the developed solar cavity receiver with 70 $kW_{th}$ nominal power can produce high-temperature air and steam simultaneously. Furthermore, the validated model can be used for the design of larger scale receivers. The stable and efficient generation of high-temperature steam and air, proven by our study, shows great potential for coupling solar cavity receivers with HTE for large-scale green hydrogen production.

Future research should include experimental and numerical studies of the developed solar cavity receiver on a demonstration plant scale (300–500 $kW_{th}$) as well as part-load operation. The design of the scaled-up solar cavity receiver must be improved for further performance enhancement (with a particular focus on reducing convective losses). Furthermore, long-term demonstration experiments and thermal stress analysis of the receiver would be necessary in future research in order to demonstrate the structural stability of the system.

## CRediT authorship contribution statement

**Yasuki Kadohiro:** Writing – original draft, Visualization, Validation, Software, Methodology, Investigation, Formal analysis, Data curation,

Conceptualization. **Timo Roeder:** Writing – review & editing, Visualization, Methodology, Investigation, Formal analysis, Data curation, Conceptualization. **Kai Risthaus:** Writing – review & editing, Supervision, Project administration, Methodology, Investigation, Formal analysis, Conceptualization. **Dmitrij Laaber:** Resources. **Nathalie Monnerie:** Writing – review & editing, Supervision, Project administration, Funding acquisition. **Christian Sattler:** Supervision, Project administration, Funding acquisition.

## Declaration of competing interest

The authors declare the following financial interests/personal relationships which may be considered as potential competing interests: Yasuki Kadohiro has patent #DE102022108479A1 pending to Deutsches Zentrum fuer Luft und Raumfahrt eV. Nathalie Monnerie has patent #DE102022108479A1 pending to Deutsches Zentrum fuer Luft und Raumfahrt eV. If there are other authors, they declare that they have no known competing financial interests or personal relationships that could have appeared to influence the work reported in this paper.

## Acknowledgments

The authors have greatly benefited from their colleagues' intellectual support. The authors thank Reiner Buck and Ralf Uhlig from Institute of Solar Research, DLR for their support using SPRAY. The authors thank Fabio Pierno, Kai-Peter Eßer, Sebastian Melzer, and Ewald-Ingo Radke from Institute of Future Fuels, DLR for their support in the preparation of the experimental setup. The authors also gratefully acknowledge the funding by the DLR internal project Solar Heat Supp. SOEC.

## Appendix A. Structure of the stainless steel housing and cavity insulation

Figs. A.1. and A.2. show the structure of stainless steel housing and cavity insulation.

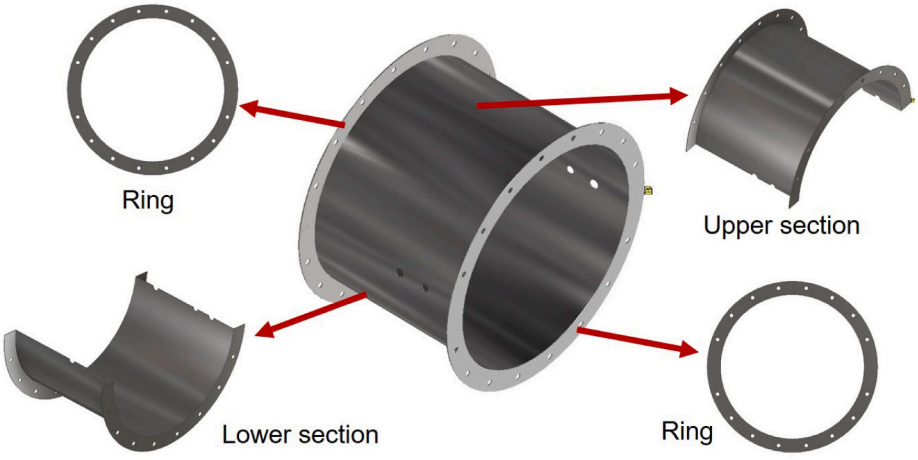


**Fig. A1.** Stainless steel housing structure.

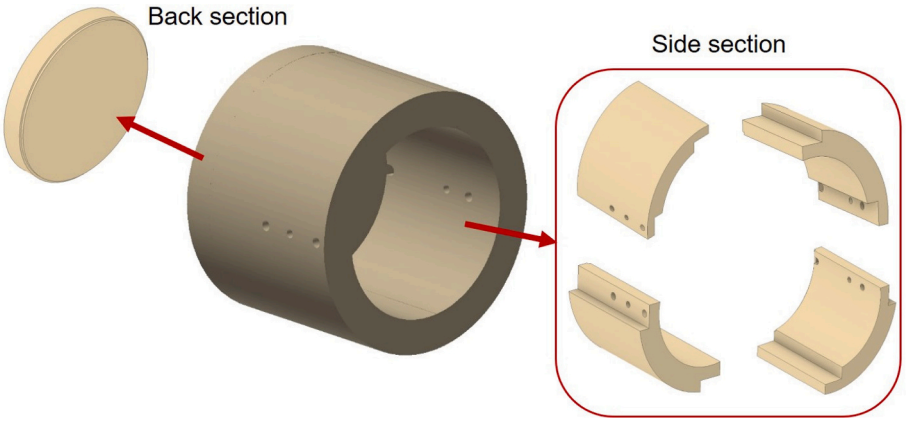


**Fig. A.2.** Cavity insulation structure.

From Fig. A.1, it can be seen that the stainless steel housing consists of upper section, lower section, and two rings. Two rings are used to fix the upper and lower section. Bolts and nuts are used for holes drilled to connect parts together. In Fig. A.2., it is shown that the cavity insulation consists of a side and back section. In addition, the side section is divided into four different parts to facilitate the construction. The z-joint shown in the side and back section is made to prevent the solar irradiation leakage from the insulation cavity and to fix each other firmly.

## Appendix B. Experimental results at nominal power on other two experimental days

Figs. B.1 and B.2 show the experimental results of fluid behavior in each AT section on other two experimental days (i) and (ii). The standard

deviation (σ), slope (S), and correlation coefficient (R) of the outlet temperature, outlet pressure, and mass flow rate of the heated steam and air in the SS and HA sections are added to the figures.

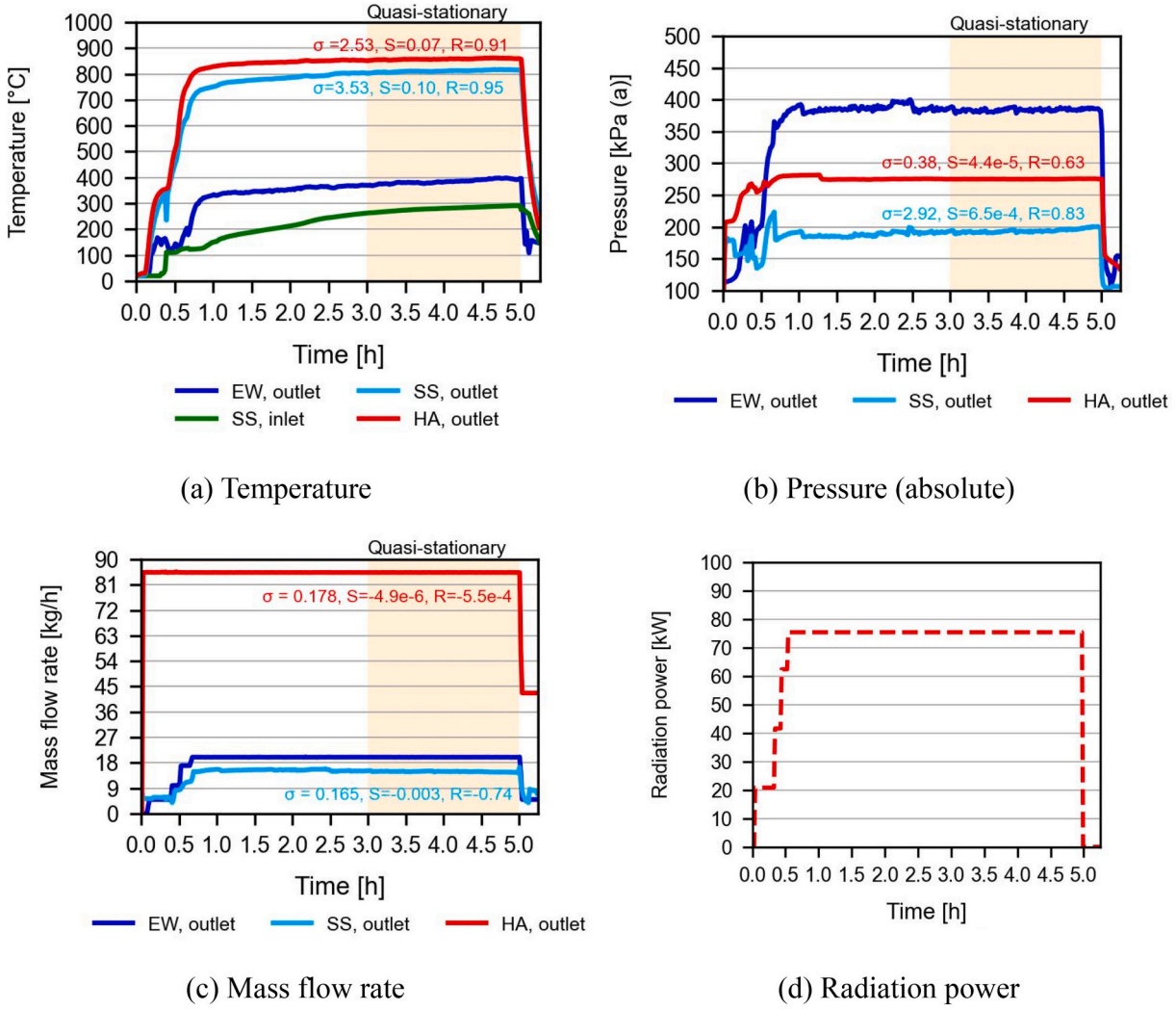


**Fig. B.1.** Experimental results of fluid behavior in each AT section – (i).

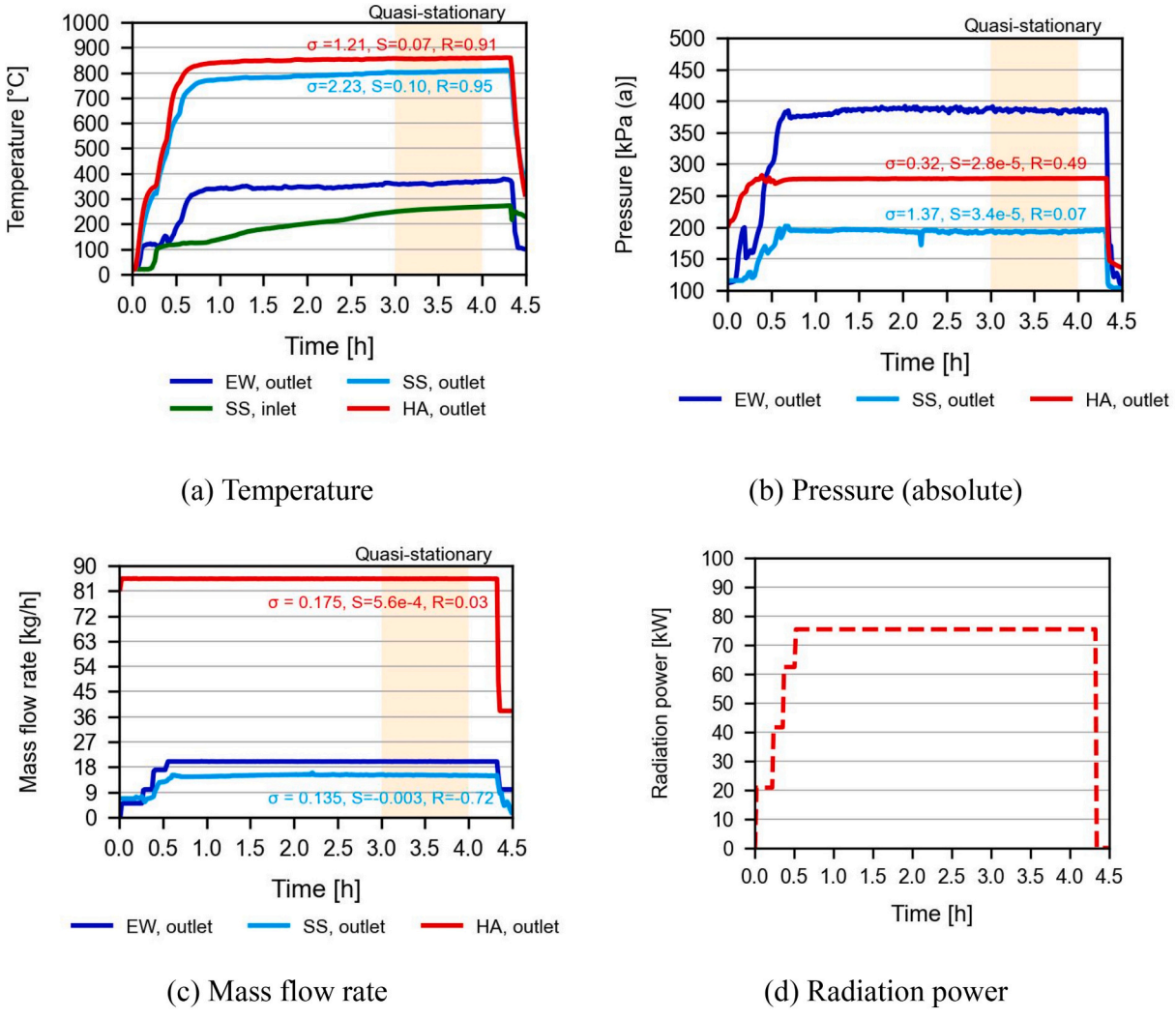


**Fig. B.2.** Experimental results of fluid behavior in each AT section – (ii).

Figs. B.3 and B.4 show the experimental results of cavity temperature on other two experimental days (i) and (ii).

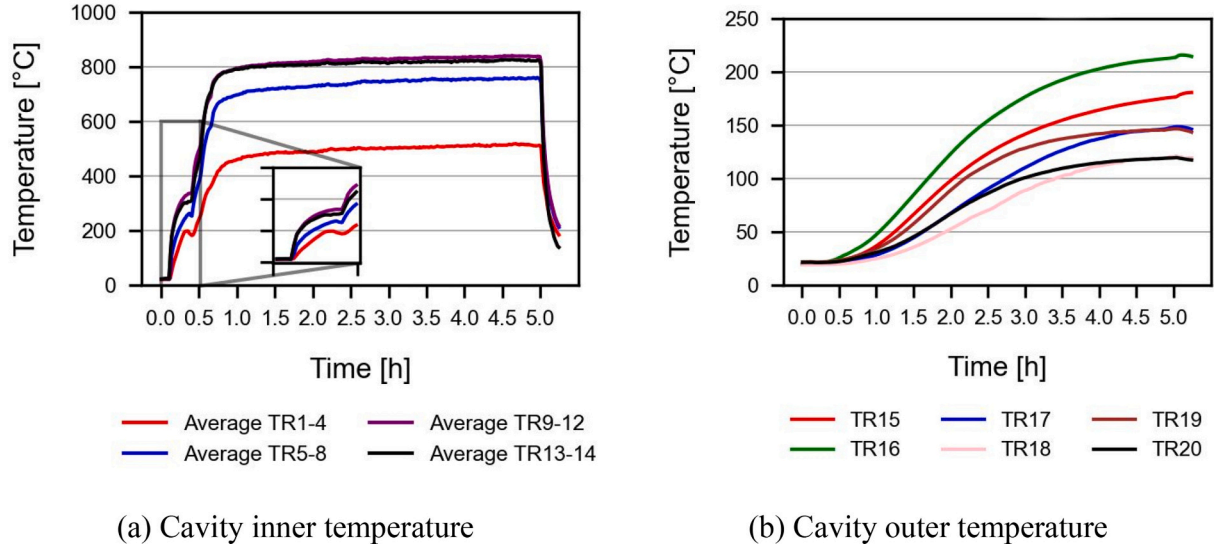


**Fig. B.3.** Experimental results of cavity temperature – (i).

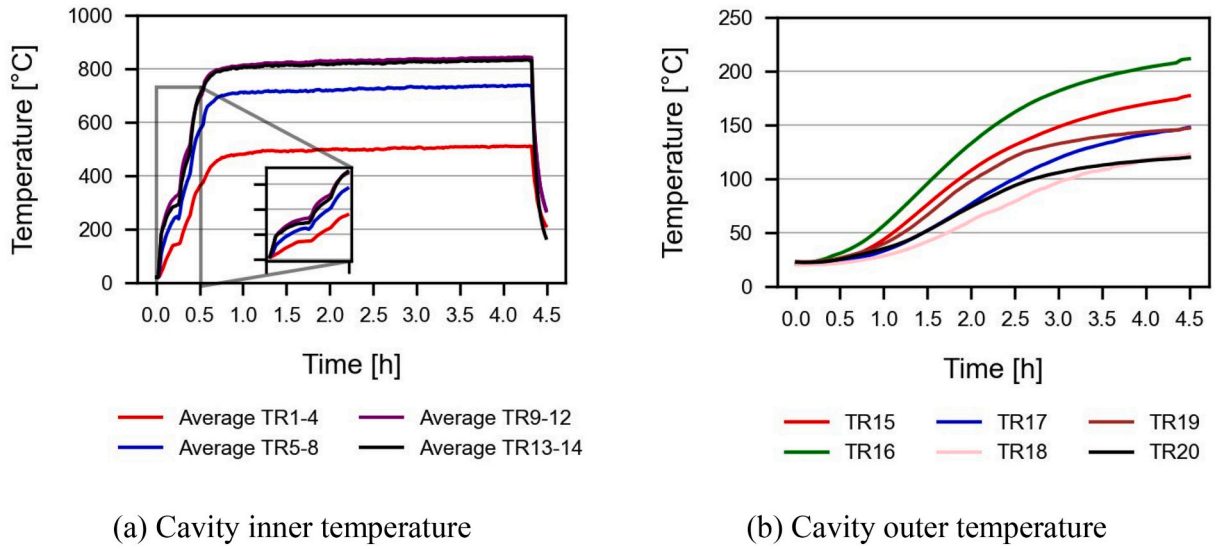


**Fig. B.4.** Experimental results of cavity temperature – (ii).

## Appendix C. Validation results on other two experimental days

Tables C.1 and C.2 show the quasi steady-state data of experiment used as inlet conditions for the numerical simulation on other two experimental days (i) and (ii). The average ambient temperature during the test on experimental dates (i) and (ii) were 28.0 °C and 28.5 °C, respectively.

**Table C.1**
Quasi steady-state data (experimental durations ranging from 3 to 5 h) of experiment used as inlet conditions for the numerical simulation – (i).

| AT section | Inlet temperature | Inlet pressure | Mass flow rate |
|---|---|---|---|
| EW | 28.1 °C | 400.9 kPa (a) | 20.0 kg/h |
| SS | 279.7 °C | 231.5 kPa (a) | 14.9 kg/h |
| HA | 20.7 °C | 306.1 kPa (a) | 85.3 kg/h |

**Table C.2**
Quasi steady-state data (experimental durations ranging from 3 to 4 h) of experiment used as inlet conditions for the numerical simulation – (ii).

| AT section | Inlet temperature | Inlet pressure | Mass flow rate |
|---|---|---|---|
| EW | 28.3 °C | 401.4 kPa (a) | 20.0 kg/h |
| SS | 260.2 °C | 231.6 kPa (a) | 15.1 kg/h |
| HA | 21.1 °C | 308.0 kPa (a) | 85.3 kg/h |

Figs. C.1 and C.2 show the comparison results of outlet fluid temperature on the other experimental days (i) and (ii). The experimental results are shown in the left bar with black dots, while the numerical results are shown in the right bar with diagonal lines. The orange line is an error bar indicating the uncertainty due to the measurement.

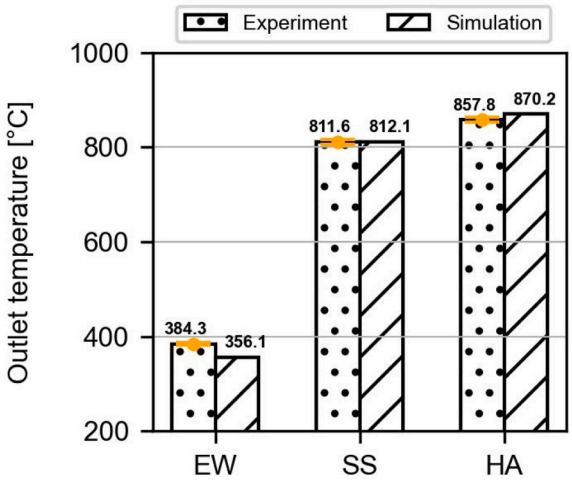


**Fig. C.1.** Comparison results of outlet fluid temperature – (i).

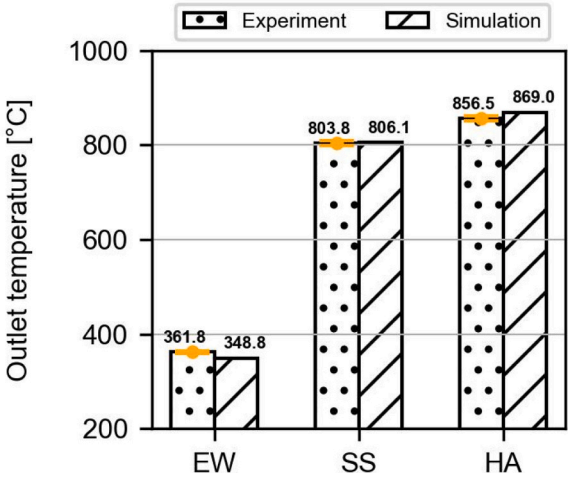


**Fig. C.2.** Comparison results of outlet fluid temperature – (ii).

As shown in the figures, there is a great agreement between the experimental and numerical results. In Fig. C.1, the errors between experiment and simulation for EW, SS, and HA sections are 7.35 %, 0.064 %, and 1.45 %, respectively. On the other hand, in Fig. C.2, the errors between experiment and simulation for EW, SS, and HA sections are 3.61 %, 0.28 %, and 1.46 %, respectively.

Figs. C.3 and C.4 show the comparison results of outlet fluid pressure on the other experimental days (ii) and (iii).

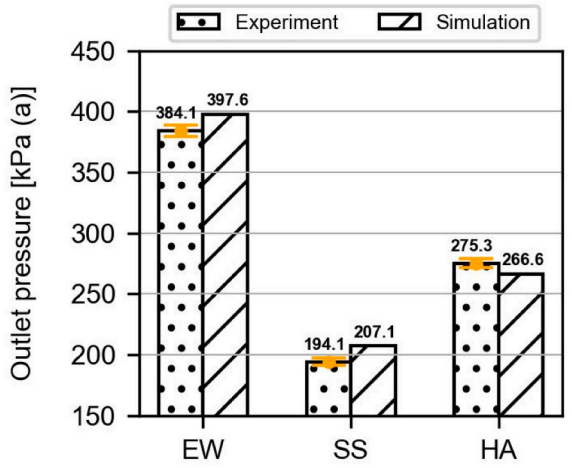


**Fig. C.3.** Comparison results of outlet fluid pressure (absolute) – (i).

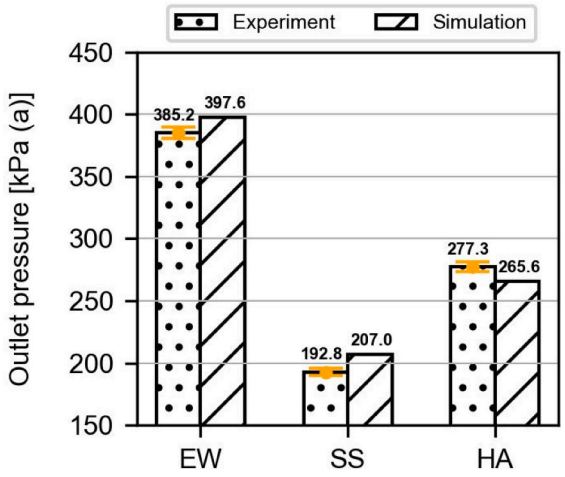


**Fig. C.4.** Comparison results of outlet fluid pressure (absolute) – (ii).

As shown in the figures, there is a great agreement between the experimental and numerical results. In Fig. C.3, the errors between experiment and simulation for EW, SS, and HA sections are 3.52 %, 6.71 %, and 3.52 %, respectively. On the other hand, in Fig. C.4, the errors between experiment and simulation for EW, SS, and HA sections are 3.23 %, 7.37 %, and 4.21 %, respectively.

Figs. C.5 and C.6 show the comparison results of lamp-to-thermal efficiency on the other experimental days (i) and (ii).

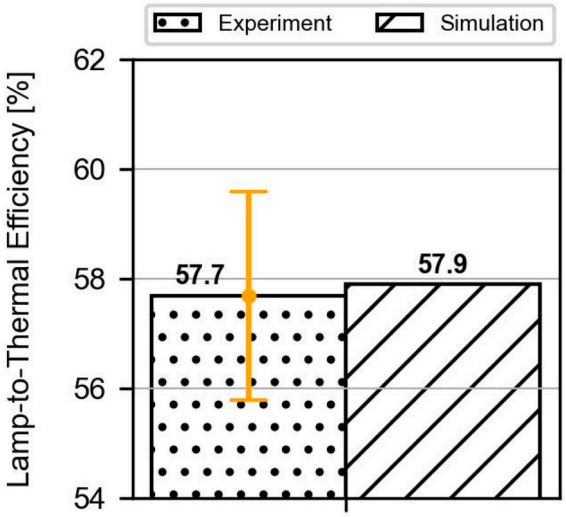


**Fig. C.5.** Comparison results of lamp-to-thermal efficiency – (i).

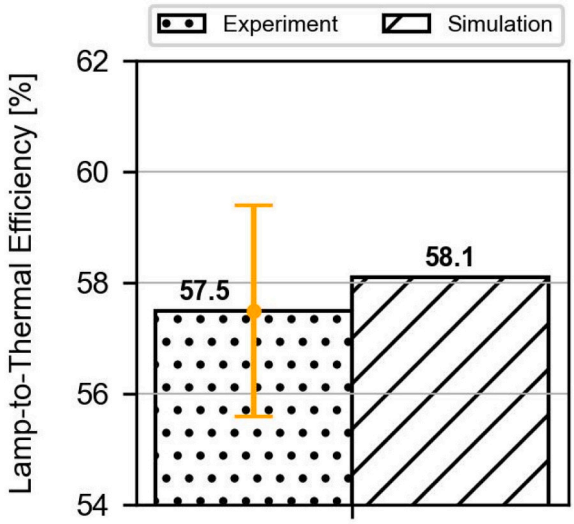


**Fig. C.6.** Comparison results of lamp-to-thermal efficiency – (ii).

As the figure shows, there is a great agreement between the experimental and numerical results. The errors between the experiment and simulation in Fig. C.5 and C.6 are 0.33 % and 0.98 %, respectively.

## Data availability

Data will be made available on request.

## References


[1] Blanco MJ, Miller S. In: Blanco MJ, Santigosa LR, editors. 1 - introduction to concentrating solar thermal (CST) technologies. Advances in Concentrating Solar Thermal Research and Technology: Woodhead Publishing Series in Energy. Woodhead Publishing; 2017. p. 3–25.

[2] Gorensek MB, Corgnale C, Summers WA. Development of the hybrid sulfur cycle for use with concentrated solar heat. I. Conceptual design Int J Hydrogen Energ 2017;42:20939–54. https://doi.org/10.1016/j.ijhydene.2017.06.241.

[3] Uygun Batgi S, Dincer I. A solar driven hybrid sulfur cycle based integrated hydrogen production system for useful outputs. Int J Hydrogen Energy 2023;48:34316–29. https://doi.org/10.1016/j.ijhydene.2023.05.199.

[4] Monnerie N, Hv Storch, Houaijia A, et al. Hydrogen production by coupling pressurized high temperature electrolyser with solar tower technology. Int J Hydrogen Energy 2017;42:13498–509. https://doi.org/10.1016/j.ijhydene.2016.11.034.

[5] Muhammad HA, Naseem M, Kim J, et al. Solar hydrogen production: Technoeconomic analysis of a concentrated solar-powered high-temperature electrolysis system. Energy 2024;298:131284. https://doi.org/10.1016/j.energy.2024.131284.

[6] Agrafiotis C, Roeb M, Sattler C. A review on solar thermal syngas production via redox pair-based water/carbon dioxide splitting thermochemical cycles. Renew Sustain Energy Rev 2015;42:254–85. https://doi.org/10.1016/j.rser.2014.09.039.

[7] Chen C, Jiao F, Lu B, et al. Challenges and perspectives for solar fuel production from water/carbon dioxide with thermochemical cycles. Carbon Neutrality 2023;2:9. https://doi.org/10.1007/s43979-023-00048-6.

[8] Perret R, Chen Y, Besenbruch G, et al. 2005 annual Progress report, IV.I.1 solar hydrogen generation research. 2005.

[9] Schiller G, Lang M, Szabo P, et al. Solar heat integrated solid oxide steam electrolysis for highly efficient hydrogen production. J Power Sources 2019;416:72–8. https://doi.org/10.1016/j.jpowsour.2019.01.059.

[10] Amaya Dueñas DM, Ullmer D, Riedel M, et al. Performance assessment of a 25 kW solid oxide cell module for hydrogen production and power generation. Int J Hydrogen Energy 2024;59:570–81. https://doi.org/10.1016/j.ijhydene.2024.01.346.

[11] Tomberg M, Heddrich MP, Ansar SA, et al. Operation strategies for a flexible megawatt scale electrolysis system for synthesis gas and hydrogen production with direct air capture of carbon dioxide. Sustainable Energy Fuels 2023;7:471–84. https://doi.org/10.1039/D2SE01473D.

[12] Buck Reiner, Schwarzbözl Peter. 4.17 solar tower systems - Dincer, Ibrahim. In: Comprehensive energy systems. Oxford: Elsevier; 2018. p. 692–732.

[13] Islam MT, Huda N, Abdullah AB, et al. A comprehensive review of state-of-the-art concentrating solar power (CSP) technologies: current status and research trends. Renew Sustain Energy Rev 2018;91:987–1018. https://doi.org/10.1016/j.rser.2018.04.097.

[14] Ho CK, Iverson BD. Review of high-temperature central receiver designs for concentrating solar power. Renew Sustain Energy Rev 2014;29:835–46. https://doi.org/10.1016/j.rser.2013.08.099.

[15] SolarPaces. CSP Projects Around the World. http://www.solarpaces.org/csp-technologies/csp-projects-around-the-world/; 2017. Accessed 25 Apr 2023.

[16] Kim J, Kim J-S, Stein W. Simplified heat loss model for central tower solar receiver. Sol Energy 2015;116:314–22. https://doi.org/10.1016/j.solener.2015.02.022.

[17] Falcone PK. A handbook for solar central receiver design. 1986.

[18] Bellos E, Bousi E, Tzivanidis C, et al. Optical and thermal analysis of different cavity receiver designs for solar dish concentrators. Energy Conversion Management: X 2019;2:100013. https://doi.org/10.1016/j.ecmx.2019.100013.

[19] Kasaeian A, Kouravand A, Vaziri Rad MA, et al. Cavity receivers in solar dish collectors: a geometric overview. Renew Energy 2021;169:53–79. https://doi.org/10.1016/j.renene.2020.12.106.

[20] Ho CK. Advances in central receivers for concentrating solar applications. Sol Energy 2017;152:38–56. https://doi.org/10.1016/j.solener.2017.03.048.

[21] Kulkarni K, Havaldar S, Bhattacharya N. Review on advance tubular receivers for central solar tower system. In: In: IOP Conference Series: Materials Science and Engineering. 1136. IOP Publishing; 2021. p. 12018.

[22] Houaijia A, Breuer S, Thomey D, et al. Solar hydrogen by high-temperature electrolysis: Flowsheeting and experimental analysis of a tube-type receiver concept for superheated steam production. Energy Procedia 2014;49:1960–9. https://doi.org/10.1016/j.egypro.2014.03.208.

[23] Quero M, Korzynietz R, Ebert M, et al. Solugas – operation experience of the first solar hybrid gas turbine system at MW scale. Energy Procedia 2014;49:1820–30. https://doi.org/10.1016/j.egypro.2014.03.193.

[24] Qiu K, Yan L, Ni M, et al. Simulation and experimental study of an air tube-cavity solar receiver. Energ Conver Manage 2015;103:847–58. https://doi.org/10.1016/j.enconman.2015.07.013.

[25] Chu S, Bai F, Zhang X, et al. Experimental study and thermal analysis of a tubular pressurized air receiver. Renew Energy 2018;125:413–24. https://doi.org/10.1016/j.renene.2018.02.125.

[26] Lin M, Suter C, Diethelm S, et al. Integrated solar-driven high-temperature electrolysis operating with concentrated irradiation. Joule 2022. https://doi.org/10.1016/j.joule.2022.07.013.

[27] Kadohiro Y, Thanda VK, Lachmann B, et al. Cavity-shaped direct solar steam generator employing conical helical tube for high-temperature application: model development, experimental testing and numerical analysis. Energy Conversion Management: X 2023;18:100366. https://doi.org/10.1016/j.ecmx.2023.100366.

[28] Kadohiro Y, Risthaus K, Monnerie N, et al. Numerical investigation and comparison of tubular solar cavity receivers for simultaneous generation of superheated steam and hot air. Appl Therm Eng 2024;238:122222. https://doi.org/10.1016/j.applthermaleng.2023.122222.

[29] Roeder T, Risthaus K, Monnerie N, et al. Non-stoichiometric redox thermochemical energy storage analysis for high temperature applications. Energies 2022;15. https://doi.org/10.3390/en15165982.

[30] Laaber D, Von Storch H, Wieghardt K, et al. One year with synlight – review of operating experience. AIP Conf Proceed 2019;2126:170007. https://doi.org/10.1063/1.5117677.

[31] Ben-Zvi R, Epstein M, Segal A. Simulation of an integrated steam generator for solar tower. Sol Energy 2012;86:578–92. https://doi.org/10.1016/j.solener.2011.11.001.
[32] He Y-L, Wang K, Qiu Y, et al. Review of the solar flux distribution in concentrated solar power: non-uniform features, challenges, and solutions. Appl Therm Eng 2019;149:448–74. https://doi.org/10.1016/j.applthermaleng.2018.12.006.
[33] Santini L, Cioncolini A, Butel MT, et al. Flow boiling heat transfer in a helically coiled steam generator for nuclear power applications. International Journal of Heat and Mass Transfer 2016;92:91–9. https://doi.org/10.1016/j.ijheatmasstransfer.2015.08.012.
[34] Gou J, Ma H, Yang Z, et al. An assessment of heat transfer models of water flow in helically coiled tubes based on selected experimental datasets. Annals Nuclear Energy 2017;110:648–67. https://doi.org/10.1016/j.anucene.2017.07.015.
[35] Willsch Christian. Receiver für Solarenergiegewinnungsanlagen sowie Solarenergiegewinnungsanlage(DE102016220522A1). https://patents.google.com/patent/DE102016220522A1/de; 2018.
[36] Helling GmbH PYROMARK. HIGH TEMPERATURE PAINT. https://helling.de/en/product/pyromark-high-temperature-paint/; 2024. Accessed 11 Jun 2024.
[37] Thelen M, Raeder C, Willsch C, et al. A high-resolution optical measurement system for rapid acquisition of radiation flux density maps. AIP Conf Proceed 2017;1850:150005. https://doi.org/10.1063/1.4984534.
[38] Thanda VK, Fend T, Laaber D, et al. Experimental investigation of the applicability of a 250 kW ceria receiver/reactor for solar thermochemical hydrogen generation. Renew Energy 2022;198:389–98. https://doi.org/10.1016/j.renene.2022.08.010.
[39] Wieghardt K, Laaber D, Dohmen V, et al. Synlight - a new facility for large-scale testing in CSP and solar chemistry. AIP Conf Proceed 2018;2033:40042. https://doi.org/10.1063/1.5067078.
[40] Uhlig R. Transient stresses at metallic solar tube receivers. 2011.
[41] Woite M. Material No.: 1.4841. https://woite-edelstahl.com/14841en.html#; 2012. Accessed 18 Jul 2022.
[42] Cheng L, Ribatski G, Thome JR. Two-phase flow patterns and flow-pattern maps: fundamentals and applications. Appl Mech Rev 2008;61. https://doi.org/10.1115/1.2955990.
[43] Brady MP, Keiser JR, More KL, et al. Comparison of short-term oxidation behavior of model and commercial Chromia-forming ferritic stainless steels in dry and wet air. Oxid Met 2012;78:1–16. https://doi.org/10.1007/s11085-012-9289-3.
[44] Wambach J, Wokaun A, Hiltpold A. Oxidation of stainless steel under dry and aqueous conditions: oxidation behaviour and composition. Surf Interface Anal 2002;34:164–70. https://doi.org/10.1002/sia.1275.
[45] ennoLogic Emissivity Table for Infrared Thermometer Readings. https://ennologic.com/wp-content/uploads/2018/07/Ultimate-Emissivity-Table.pdf; 2024. Accessed 24 May 2024.
[46] Amsbeck L, Denk T, Ebert M, et al. Test of a solar-hybrid microturbine system and evaluation of storage deployment. 2010.
[47] Wang K, Wu H, Wang D, et al. Experimental study on a coiled tube solar receiver under variable solar radiation condition. Sol Energy 2015;122:1080–90. https://doi.org/10.1016/j.solener.2015.10.004.
[48] Zhu J, Wang K, Wu H, et al. Experimental investigation on the energy and exergy performance of a coiled tube solar receiver. Appl Energy 2015;156:519–27. https://doi.org/10.1016/j.apenergy.2015.07.013.
[49] Swanepoel JK, Le Roux WG, Lexmond AS, et al. Helically coiled solar cavity receiver for micro-scale direct steam generation. Appl Therm Eng 2021;185:116427. https://doi.org/10.1016/j.applthermaleng.2020.116427.